Check for updates

JGR Atmospheres

RESEARCH ARTICLE
10.1029/2021JD034992

Key Points:

- Aqueous-phase chemistry processes cause aerosol populations to be more internally mixed
- The change of aerosol mixing state due to aqueous phase chemistry was related to the fraction of activated particles
- Coagulation within clouds has a negligible impact on aerosol mixing state

Supporting Information:

Supporting Information may be found in the online version of this article.

Correspondence to:

N. Riemer,
nriemer@illinois.edu

Citation:

Yao, Y., Dawson, M. L., Dabdub, D., & Riemer, N. (2021). Evaluating the impacts of cloud processing on resuspended aerosol particles after cloud evaporation using a particle-resolved model. *Journal of Geophysical Research: Atmospheres*, *126*, e2021JD034992. https://doi.org/10.1029/2021JD034992

Received 31 MAR 2021
Accepted 19 NOV 2021

© 2021. American Geophysical Union. All Rights Reserved.

Evaluating the Impacts of Cloud Processing on Resuspended Aerosol Particles After Cloud Evaporation Using a Particle-Resolved Model

Yu Yao[1], Matthew L. Dawson[2,3], Donald Dabdub[3], and Nicole Riemer[1]

[1]Department of Atmospheric Sciences, University of Illinois at Urbana-Champaign, Urbana, IL, USA, [2]Now at National Center for Atmospheric Research, Boulder, CO, USA, [3]Department of Mechanical and Aerospace Engineering, University of California, Irvine, CA, USA

Abstract Aerosol particles undergo physical and chemical changes during cloud processes. In this work, we quantified the changes in aerosol mixing state using a particle-resolved model. To this end, we coupled the particle-resolved aerosol model PartMC-MOSAIC with the aqueous chemistry module CAPRAM 2.4 and designed cloud parcel simulations that mimicked several cloud cycles that a particle population may be exposed to in polluted urban environments. With ammonium nitrate and ammonium sulfate added to the activated particles, after the cloud evaporated, the activation potential of the resuspended aerosol particles increased for supersaturation thresholds lower than the maximum supersaturation attained in the cloud. Formation of sulfate and nitrate increased the internally mixed state of all particle populations, quantified by the mixing state index χ. The change of aerosol mixing state due to aqueous-phase chemistry was related to the fraction of activated particles. For a case with low aerosol number concentration, where the activated fraction was up to 60%, χ increased by up to 50 percentage points after cloud processing, reaching an almost completely internal mixture. In contrast, for a case with high aerosol emissions and activated fraction of less than 20%, the increase in χ was less than 20 percentage points, and χ remained below 80% after cloud processing. The change in aerosol mixing state caused by coagulation within the cloud parcel was negligible. These findings highlight the complex influence of cloud processing on particle properties.

Plain Language Summary Every cloud droplet contains at least one aerosol nucleus. The composition and mass of this nucleus can be changed during a cloud's lifetime by several chemical and physical processes. Once the cloud evaporates, a modified aerosol population is released into the atmosphere compared to the population that formed the cloud, which may also have different impacts on climate. In this work, we used a particle-resolved process model to study the effects of cloud processing on aerosols within clouds. This modeling approach is suitable for this research because each particle is tracked individually, which allows us to quantify changes in particle composition without simplifying assumptions, such as averaging composition within predescribed size ranges. Because of the formation of ammonium sulfate and nitrate in the cloud, particles that formed cloud droplets grew larger and were more likely to form cloud droplets in future cloud cycles. Overall, cloud processing by aqueous-phase chemistry produced aerosol populations where the particles look more similar to each other in composition.

1. Introduction

Atmospheric aerosol particles are complex mixtures of different chemical species, reflecting the fact that they originate from different emission sources and experience various aging processes in the atmosphere (Riemer et al., 2009; Li et al., 2011; Bondy et al., 2018; Healy et al., 2014; Rissler et al., 2014). Aging processes include processes in the cloud-free atmosphere such as coagulation, heterogeneous reactions on the particles' surface, and the formation of coatings from organic and inorganic secondary aerosol. They also include processes in clouds (Lance et al., 2017) such as aqueous-phase chemistry within cloud droplets forming inorganic and organic aerosol material and collision coalescence of particles and droplets within a cloud. When clouds evaporate, aerosol populations are released into the atmosphere with modified properties compared to the populations that formed the cloud. This, in turn, changes the aerosols' impacts on clouds in the next cloud cycle (Hoose et al., 2008), and therefore, this process is important for 3D chemical transport models to include. At the same time, it poses challenges to be represented in chemical transport models (Gao et al., 2016).

Specifically, in-cloud processes have been shown to produce a double-peaked size distribution since material from the gas phase and from smaller particles is transferred to the accumulation mode size range (Hoppel et al., 1986; Noble & Hudson, 2019). It has also been observed that cloud droplets of different sizes may differ in their acidity (Collett et al., 1994; Pye et al., 2020). This has important implications for the rates of aqueous-phase sulfate formation (Hoag et al., 1999), which depends strongly on pH, and this needs to be considered when representing these processes in cloud microphysics models (Hegg & Larson, 1990; Barth, 2006). Because of the nonlinearity of aqueous chemistry processes, models predict larger rates of sulfate formation when using a more realistic size-resolved droplet representation compared to using a prescribed single droplet size.

In this study, we not only considered the variation of aerosol (and cloud droplet) composition with size, but also the variation of composition within a narrow size range, commonly referred to as mixing state (Winkler, 1973; Riemer et al., 2019). Our goal in this study was to quantify the changes in aerosol mixing state due to in-cloud aqueous-phase chemistry and coagulation processes. Aerosol mixing state impacts the aerosols' effects on health (Ching & Kajino, 2018), their absorption and scattering of sunlight (Lesins et al., 2002; Fierce et al., 2020), and their ability to act as cloud condensation and ice nuclei (Broekhuizen et al., 2006; Bhattu & Tripathi, 2015; Knopf et al., 2018).

On one hand, mixing state is a factor that determines which particles activate and form cloud droplets, thereby determining cloud properties (Ching et al., 2012; Ching et al., 2016). On the other hand, mixing state can be modified by in-cloud processes. For example, observations using online single-particle mass spectrometry during the HCCT-2010 field campaign showed that cloud residuals contain more sulfate and nitrate compared to the below-cloud aerosol (Roth et al., 2016), resulting in a change of aerosol mixing state.

Model simulations of aerosol mixing state are challenging and particularly rare when it comes to simulating in-cloud processes due to the need for extensive computing resources. Regional or global models use simplified assumptions about aerosol activation and aerosol mass and size changes due to cloud processing, which are determined by the underlying model representation of aerosol and cloud droplets. For example, in the CMAQ model, which uses a modal aerosol representation, the sulfate mass produced by in-cloud chemistry is added to the entire accumulation mode (Ervens, 2015; Fahey et al., 2017). In the global climate model ECHAM5-HAM, activated particles are grouped into two bins, one with low ion concentration and the other with higher ion concentration (Roelofs et al., 2006) to capture the dependence of the sulfate formation pathway on pH.

High-resolution cloud models typically use a size-resolved fixed-bin microphysical model (Flossmann, 1994; Feingold et al., 1996) and resolve aerosol particles and cloud droplets by separate distributions, thus internally mixing all same-sized particles or droplets. Similarly, accurate parcel models most frequently use a size-resolved moving-bin approach (Kreidenweis et al., 2003; Cooper et al., 1997), again losing aerosol history and composition information within each size bin. To preserve some composition information, 2D aerosol models have been used, resolving cloud droplet size and aerosol dry volume (Bott et al., 1996; Ovchinnikov & Easter, 2010). However, increasing the dimension beyond 2D to treat composition variation of the aerosol in more detail would be computationally prohibitively expensive. Lagrangian cloud microphysics models have also been developed that track information on a droplet level (Shima et al., 2009; Andrejczuk et al., 2008; Grabowski et al., 2019; Sölch & Kärcher, 2010; Unterstrasser & Sölch, 2014; Jaruga & Pawlowska, 2018). However, their focus has been the study of cloud microphysics rather than the modification of aerosol composition. While Jaruga and Pawlowska (2018) consider some aqueous-phase chemistry processes, their representation of the aerosol is comparatively simple and questions about mixing state have not yet been addressed.

For our study, we used the aerosol model PartMC-MOSAIC (Particle Monte Carlo-Model for Simulating Aerosol Interactions and Chemistry) (Riemer et al., 2009; Zaveri et al., 2008) as aerosol and cloud parcel model. This stochastic particle-resolved model explicitly resolves the composition of individual aerosol particles and cloud droplets in a given population. Since individual particles and droplets are explicitly tracked, there is no need to invoke ad hoc aging criteria that move aerosol mass between bins or modes as is the case with traditional modal or sectional approaches (Riemer et al., 2003; Stier et al., 2005; Bauer et al., 2008; Jacobson, 2001). Tracking droplets explicitly is therefore well-suited to simulate aerosol mixing state and investigate its impacts on climate-relevant aerosol properties.

The model was described in Ching et al. (2012) and Ching et al. (2016) and has been used to simulate the mixing state evolution of black-carbon-containing aerosol in the cloud-free atmosphere, followed by a process analysis

to what extent the aged aerosol is able to undergo nucleation-scavenging as the particles compete for water vapor in an updraft. However, these studies did not include the effects of aqueous-phase chemistry occurring within the cloud droplets. This is the motivation for this study, where we extended our modeling framework to include aqueous-phase chemistry within the cloud droplets that are forming on a diverse population of particles, common to urban environments. The contribution of this paper is the first study to document quantitatively the impact of aqueous-phase chemistry on mixing state.

We focused on the following questions: (1) To what extent does cloud processing change the aerosol mixing state of the population that entered the cloud? (2) How does this change the cloud condensation number concentration? (3) What is the role of coagulation between the interstitial particles and cloud droplets for mixing state of the aerosol?

Section 2 describes the model components, the scenario setup, and the mixing state metrics used in this study. Section 3 presents the analysis of the simulation results. Section 4 summarizes our results.

2. Model Description and Metrics

2.1. Stochastic Particle-Resolved Module PartMC-MOSAIC

Aerosol physical and chemical processes were simulated by the stochastic particle-resolved model PartMC-MOSAIC (Particle Monte Carlo-Model for Simulating Aerosol Interactions and Chemistry-Model for Simulating Aerosol Interactions and Chemistry, Riemer et al., 2009; Zaveri et al., 2008). The PartMC model simulates the evolution of per-particle composition of a large ensemble of computational particles in a well-mixed computational volume. In contrast to Lagrangian droplet models that have become popular in the cloud microphysics community (Shima et al., 2009; Grabowski et al., 2019), PartMC-MOSAIC does not track the position of particles and droplets within the computational volume.

The particle number concentration changes due to coagulation, emission, and dilution, which are simulated by using a stochastic Monte Carlo sampling method (Riemer et al., 2009). Gas-phase chemistry and gas-particle partitioning are represented by the aerosol chemistry model MOSAIC, which includes CBM-Z for gas-phase photochemical reactions (Zaveri, 1999), MTEM for estimating mean activity coefficient of an electrolyte in an inorganic multicomponent solution (Zaveri, Easter, & Wexler, 2005), and MESA for intraparticle solid-liquid partitioning for inorganic aerosols (Zaveri, Easter, & Peters, 2005). The formation mechanism of secondary organic aerosol (SOA) in MOSAIC is based on SORGAM (Schell et al., 2001) with several parameters adjusted to bring the simulated values closer to observation (Zaveri et al., 2010). The model represents key aerosol species, including sulfate, nitrate, ammonium, black carbon (BC), primary organic aerosol (POA), and several surrogate secondary organic aerosol (SOA) species. The coupled model PartMC-MOSAIC was applied in previous studies for simulating aerosol optical and CCN properties, black carbon aging timescales, and the black carbon absorption enhancement due to the coatings (Zaveri et al., 2010; Riemer et al., 2010; Fierce et al., 2017, 2020), focusing on mixing state evolution during cloud-free conditions. The model was also used for evaluating the impact of aerosol mixing state on cloud droplet formation (Ching et al., 2012; Ching et al., 2016), which will be explained in more detail in the next section.

2.2. Cloud Parcel Model and Aqueous-Phase Chemistry

Ching et al. (2012) described the details of the particle-resolved cloud parcel model, which simulates a population of aerosol particles that experience cooling at a prescribed cooling rate and subsequent growth due to the condensation of water vapor. The condensational growth of the particles is calculated following Seinfeld and Pandis (2006). The driving force of the growth is the difference between droplet equilibrium saturation vapor pressure and the ambient vapor pressure of the environment. The equilibrium saturation vapor pressure is calculated by Köhler theory, and the particle hygroscopicity is determined using the parameterization of aerosol hygroscopicity developed by Petters and Kreidenweis (2007). The hygroscopicity κ of each particle is calculated by using the volume-weighted average of the individual κ values of the particles' constituent species. We used κ of 0.65 for ammonium sulfate and ammonium nitrate, κ of 0.1 for SOA, and κ of 0.001 for POA. BC is assumed to be hyrophobic and has κ of 0. The hygroscopicity of each particle varied as the chemical composition evolved

for each particle. We currently do not represent any entrainment of cloud-free air into the cloud, surface tension effects on droplet growth, or the loss of droplets from the air parcel owing to sedimentation.

The aim of this paper is to investigate the impacts of in-cloud aqueous-phase chemistry on aerosol mixing state. To this end, we coupled the reduced Chemical Aqueous Phase Radical Mechanism (CAPRAM) 2.4 to PartMC-MOSAIC. The reduced CAPRAM model includes 183 reactions (including Henry's Law partitioning, dissociation reactions, photolysis reactions, and other aqueous-phase reactions) and 113 species (Ervens et al., 2003). The mechanism treats the reactions of common radicals and radical anions, transition metal ions, and organics with less than two carbon atoms. The CAPRAM mechanism was applied to simulate the cloud processes for the FEBUKO field campaign and reproduced the aqueous sulfate and organic compounds oxidation processes well (Tilgner et al., 2005; Wolke et al., 2005). While the aqueous-phase chemistry involving transition metal ions and organic species is of great interest (Mayol-Bracero et al., 2002; Harris et al., 2013; Alexander et al., 2009; Lian et al., 2019; McNeill, 2015; Smith et al., 2014; Wonaschuetz et al., 2012; Wagner et al., 2015), our scope for this initial study is the in-cloud production of sulfate and nitrate and their relationship to changes in aerosol mixing state. We did not consider the co-condensation of nitric acid gas due to vapor pressure difference discussed by Crooks et al. (2018). A subset of the most relevant Henry's law constants, aqueous equilibria, and chemistry reactions are summarized in Table S1 in the Supporting Information S1.

The original gas-phase chemistry mechanism Regional Atmospheric Chemistry Modeling (RACM) used in CAPRAM 2.4 was replaced with CBM-Z, which is the gas-phase mechanism native to PartMC-MOSAIC. In the current setting, aqueous chemistry and the evaporation and condensation of gases (other than water vapor) to aqueous particles are enabled for particles with liquid water mass larger than 5×10^{-16} kg, which corresponds to solution droplets of 1 μm in diameter.

We used the CVODE (Cohen et al., 1996) solver of the SUNDIALS (Hindmarsh et al., 2005) package to solve the mass transfer and aqueous chemistry of the CAPRAM 2.4 reduced mechanism with the Backward Differentiation Formulas (BDF) and Newton Iteration, which is suitable for mathematically stiff systems, such as those treating multiphase chemistry. To reduce the stiffness of the system, the Henry's Law partitioning of the strong acids H_2SO_4, HCl, and HNO_3 was combined with their first acid dissociation step.

2.3. The Scenario Settings

The scenario setting of this work followed the two-step method used in Ching et al. (2012). Step 1 represented the simulation of an "urban plume scenario" in a subsaturated (RH < 100%) environment using PartMC-MOSAIC. The purpose of this step was to generate aerosol populations that cover a wide range of mixing states, which can later serve as input populations for our cloud parcel simulations. The urban plume simulation had a simulation time of 24 h, and the state of the aerosol and gas phase were saved hourly. This hourly output was then used as inputs for 25 separate 30-min particle-resolved cloud parcel simulations (Step 2). Each of the 25 cloud parcel simulations was exposed to the same cooling rate but differed in their initial conditions of aerosol populations and gas-phase concentrations.

The urban plume case environment shown here was adopted from Zaveri et al. (2010), following a Lagrangian box modeling approach, where we assumed that the air parcel containing background air moved over a polluted urban environment. We refer to this case for the remainder of the paper as the "high-emission" case. The initial condition of the aerosol consisted of two lognormal modes, with the number concentration, geometric mean diameter, standard deviation, and composition for each mode as listed in Table 1. We used 10,000 computational particles to resolve the initial aerosol. Note that the number of computational particles changed over the course of the simulation depending on coagulation, particle emissions, and dilution with the background, but was kept between half and double the initial number of computational particles using doubling and halving procedures as described in Riemer et al. (2009).

Gas-phase initial conditions were set to 50 pbb ozone and low levels of other trace gases. The plume was diluted with background air at a rate of 1.5×10^{-5} s^{-1} that contained the same gas mixing ratios and aerosol concentrations as the initial condition. The simulation started at 6 AM local time and lasted for 24 h with gas and aerosol emission entering the simulation during the first 12 h. We use the term "plume time," t_u, to refer to the elapsed time during this 24-h simulation in cloud-free conditions. The temperature was prescribed as shown in Figure 1. For simplicity, we assumed that the temperature remained constant after the first 6 h. This is consistent with

Table 1
Size Distributions and Compositions of Initial, Background, and Emitted Aerosols for the High-Emission Case

Initial/Background	N (cm^{-3})	D_g (μm)	σ_g	Composition by mass	D_i[b]
Aitken mode	1800	0.02	1.45	49.6% $(NH_4)_2SO_4$ + 49.6% API1[a] + 0.8% BC	2.08
Accumulation mode	1500	0.116	1.65	49.6% $(NH_4)_2SO_4$ + 49.6% API1 + 0.8% BC	2.08
Emission	E ($m^{-2}s^{-1}$)	D_g (μm)	σ_g	Composition by mass	D_i
Cooking	9×10^6	0.086	1.91	100% POA	1
Diesel	1.6×10^8	0.05	1.74	70% BC + 30% POA	1.84
Gasoline	5×10^7	0.05	1.74	20% BC + 80% POA	1.65

[a]Low volatility secondary aerosol product from the oxidation of α-pinene. [b]Per-particle diversity, refer to Section 2.4 for a detailed description.

the air parcel staying in the fully matured mixed layer until sunset and in the residual layer thereafter (Zaveri et al., 2010). The resulting relative humidity varied between 52% and 95%, assuming that the total water content in the air parcel was constant.

Aerosol emission sources and their compositions are also listed in Table 1. Note that the composition of aerosol emissions from gasoline vehicles was based on Somers (2004) and Nam et al. (2008). Current gasoline vehicles produce tailpipe emissions with higher BC content (Liggio et al., 2012). However, since both BC and POA have very low hygroscopicities ($\kappa = 0$ for BC and 0.001 for POA), we do not expect that the exact BC/POA split impacted our results for this paper (however, this will be important for optical properties).

The mixing state of the aerosol in this simulation evolved because primary aerosol emissions aged owing to the formation of secondary aerosol and to coagulation processes, while fresh emissions continued to enter during the first 12 hours of simulation. Overall, this scenario mimicked the evolution of an air parcel in a polluted urban area, and we summarized the results, including the mixing state evolution in Section 3.1. The full state, including gas-phase mixing ratios and composition of all computational particles, was saved hourly to be used as input for the cloud parcel simulations in step 2.

In addition to the high-emission urban plume case described above, we performed a second simulation with reduced initial aerosol number concentration and aerosol emissions (5% of the high-emission case) and gas emissions (15% of the high-emission case) to represent a less polluted urban environment. We refer to this case as the "low-emission case." Scale parameters relative to the high-emission case are summarized in Table 2.

For step 2, the hourly output of the simulated aerosol and gas-phase mixing ratios was used as input for the cloud parcel simulations, using a prescribed cooling rate. The temperature decreased for the first 10 minutes at a rate of 0.25 K min^{-1}, which corresponds to an updraft velocity of approximately 1 m s^{-1}. The value is calculated by using equation (17.56) in Seinfeld and Pandis (2006) without consideration of entrainment. The cooling rate was

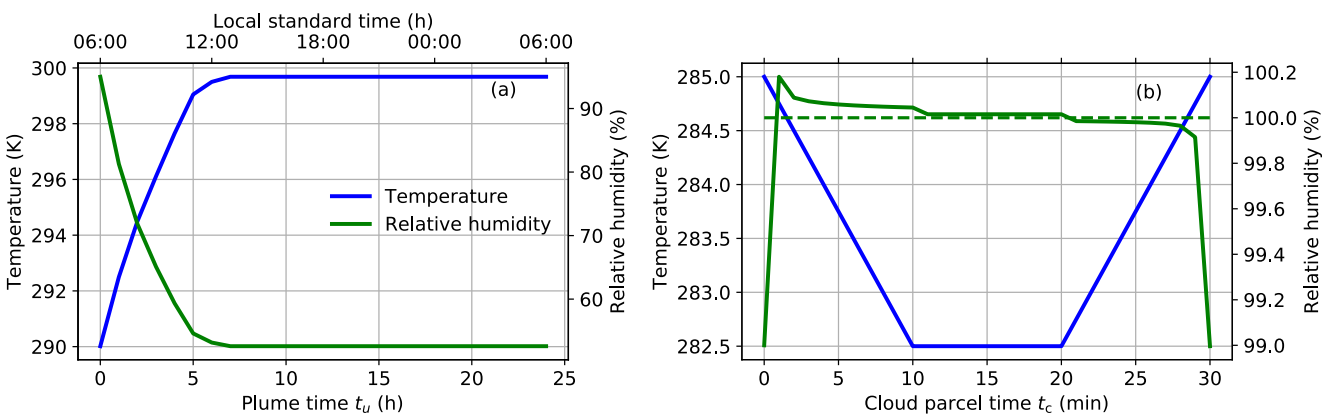


Figure 1. Temperature and relativity humidity time series in (a) urban plume environment and (b) cloud parcel environment. The green-dashed line in (b) is RH = 100%.

Table 2
Scale Parameters of Gas Emission Rates, Initial and Background Particle Number Concentration, and Aerosol Number Fluxes Emission Rates Used for Low-Emission Cases (Relative to High-Emission Case)

		Initial/background number conc.		Aerosol emission rates		
	Gas emission rates	Aitken	Accumulation	Cooking	Diesel	Gasoline
Scale parameters	15%	5%	5%	5%	5%	5%

kept constant for the next 10 minutes and increased at the rate of 0.25 K min^{-1} for the last 10 minutes. Hence, one cloud cycle consisted of a total of 30 minutes, and we referred to the elapsed time within the cloud cycle as "cloud parcel time," t_c. The initial RH for the cloud parcel was 99%, and it reached supersaturation within less than 1 min. The parcel became subsaturated when the cloud began to evaporate at 20 min and returned to RH = 99% at the end of the simulation.

Since it is common for air parcels to undergo several cloud cycles (Barth et al., 2003), we conducted a total of four cloud cycles for the high-emission case, which resulted in a total of $25 \times 4 = 100$ cloud parcel simulations. We initialized the aerosol for the second, third, and fourth cloud cycles using the particle population from the end of the previous cloud cycle. For the gas-phase mixing ratios, we always used the values from the beginning of the first cloud cycle. That is, in choosing this setup, we explored how an already processed aerosol population changes further when it is exposed to a given gas environment and cooling rate (especially focusing on changes in the mixing state) with the only difference between cloud cycles being the input aerosol population. We realize that this is an idealized setup since in reality the gas phase concentrations are likely not the same for subsequent cloud cycles. For the low-emission case, we only present the results for one cloud cycle.

Lastly, to explore the effects of coagulation, we performed another set of cloud parcel simulations that included Brownian coagulation, using the high-emission case as input. For most of our analysis, we focus on the difference between the particles at the start and the end of the cloud parcel simulations after cloud evaporation.

2.4. Mixing State Metrics

The objective of this paper is to quantify the change of particle mixing state as a result of cloud processing. The metrics used to quantify mixing state were developed by Riemer and West (2013). The mixing state metric χ is calculated by

$$\chi = \frac{D_\alpha - 1}{D_\gamma - 1}, \tag{1}$$

where D_α is the average particle diversity and D_γ is the bulk particle diversity.

The calculation of these diversity metrics is based on the per-particle mixing entropy H_i. For an aerosol population of N particles containing A species, the mixing entropy H_i and particle diversity D_i of particle i are calculated as

$$H_i = \sum_{a=1}^{A} -p_i^a \ln p_i^a \qquad D_i = e^{H_i}, \tag{2}$$

where p_i^a is the mass fraction of species a in particle i. Expanding D_i to the whole population, D_α and D_γ are defined as

$$H_\alpha = \sum_{i=1}^{N} p_i H_i \qquad D_\alpha = e^{H_\alpha}, \tag{3}$$

$$H_\gamma = \sum_{a=1}^{A} -p_a \ln p_a \qquad D_\gamma = e^{H_\gamma}, \tag{4}$$

where p_i and p_a are the mass fractions of particle i and species a in the population. For externally mixed populations where particles contain only one species, $D_\alpha = 1$ and $\chi = 0\%$. For internally mixed population where each particle has the same composition as the bulk, $D_\alpha = D_\gamma$ and $\chi = 100\%$. In the ambient atmosphere, aerosols are

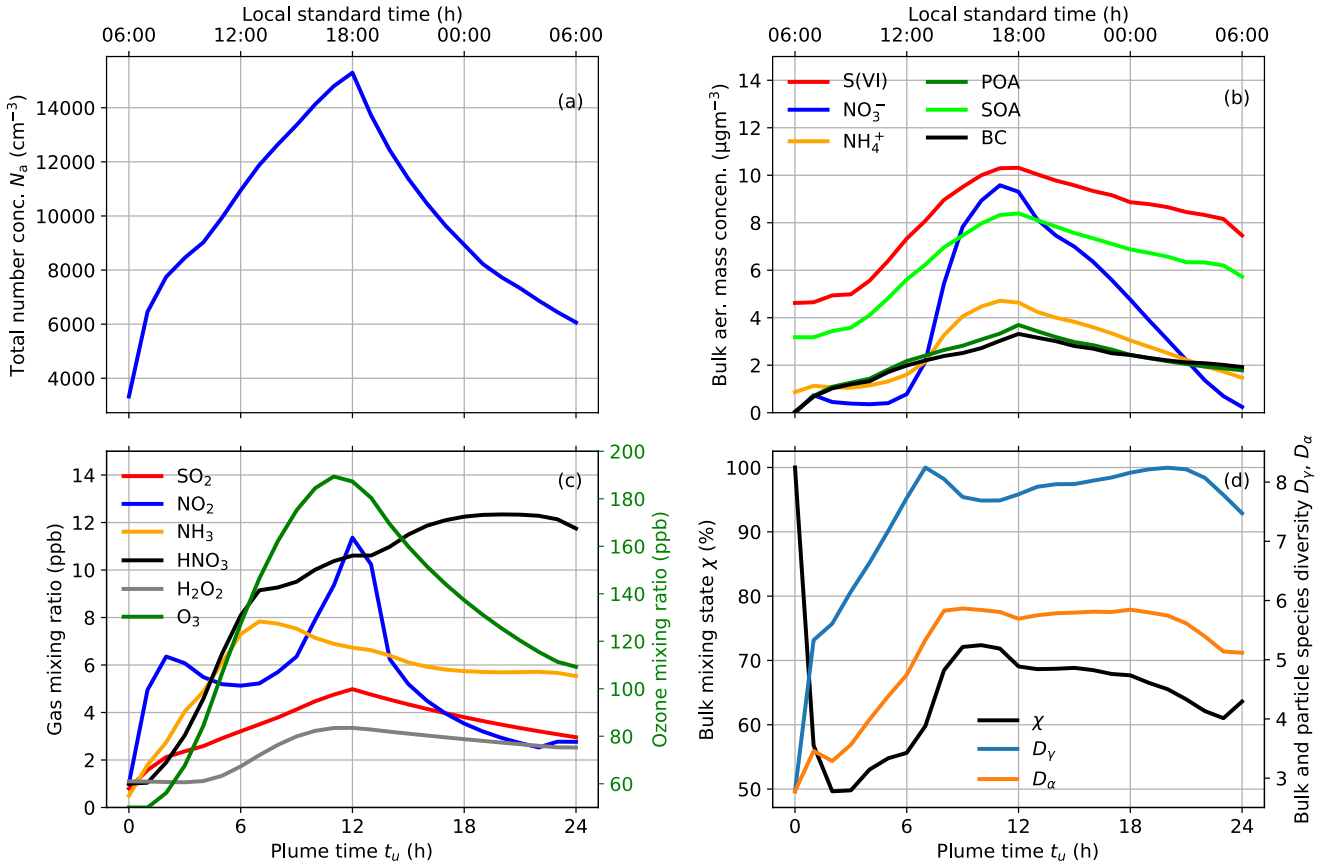


Figure 2. Temporal variation of (a) total number concentration, (b) mass concentrations of selected aerosol species, (c) mixing ratios of selected gas-phase species, and (d) aerosol mixing state metrics for the high-emission case.

neither completely internally nor externally mixed and intermediate mixing states are common (Healy et al., 2014; Ye et al., 2018; Ching et al., 2019). For regions close to emission sources, χ is expected to be lower, while χ is larger in air masses dominated by an aged aerosol.

The mixing state metrics χ defined in this paper used the abundance of model chemical species as the basis for calculating particle mass fractions in Equations 2–4, i.e., sulfate, nitrate, ammonium, POA, etc., excluding aerosol water. Other choices for defining "species" are possible, for example, Ching et al. (2017) used two surrogate species, hygroscopic and nonhygroscopic species, as the basis for χ. Furthermore, Zheng et al. (2021) compared χ based on the mixing of model chemical species, of hygroscopic and nonhygroscopic species, and of absorbing and nonabsorbing species.

3. Simulation Results

3.1. Urban Plume Simulation With PartMC-MOSAIC

This section summarizes the results from the urban plume simulations to provide context for the cloud parcel simulations discussed in the remainder of the paper. Figure 2 shows selected quantities from the high-emission urban plume simulation. The total particle number concentration N_a increased initially due to the emission of primary particles, reached a maximum of 15,295 cm^{-3} at t_p = 12 h, then decreased because the emissions ceased, and both dilution and coagulation reduced the particle number concentration. Similarly, BC and POA mass concentrations increased for the first 12 h due to emission and decreased thereafter due to dilution with the background, just as shown in Figure 2b. The time series of the secondary aerosol species sulfate and SOA were determined by the interplay of loss by dilution and photochemical production. The ammonium nitrate mass concentration was determined by the gas concentrations of its precursors, HNO_3 and NH_3, temperature, and RH. Mixing ratios of SO_2,

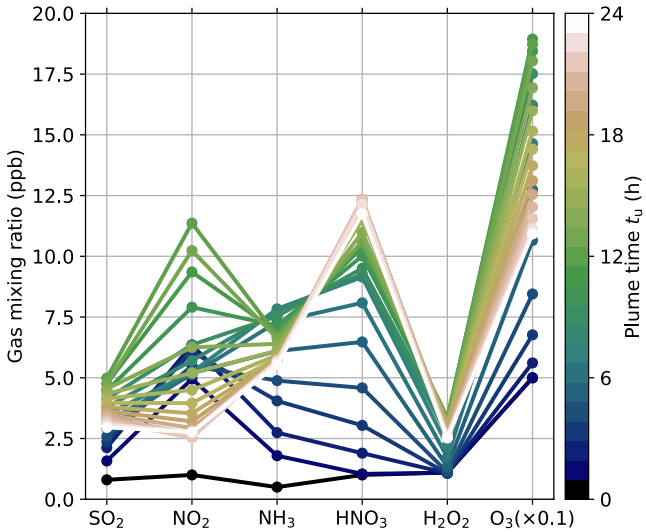


Figure 3. Initial conditions for the selected gas-phase species for the cloud parcel simulations (high-emission case). Colors indicate the different plume hours. Note that the mixing ratio for O_3 is multiplied by 0.1 to be able to use the same scale on the ordinate as for the other gases.

O_3, and H_2O_2 are shown in Figure 2c for reference because they are directly involved in the in-cloud sulfate formation as discussed in Section 3.2.

Figure 2b only displays the bulk composition of the aerosol, while the mixing state information available from the particle-resolved output remains hidden. Figure 2d provides insight into the evolution of aerosol mixing state as quantified by the mixing state metrics introduced in Section 2.4. At $t_u = 0$, the particle population was completely internally mixed, and therefore, the mixing state index χ was initially 100%.

From Equation 1, we recall that χ is determined by the ratio of D_α and D_γ. Figure 2d indicates that both D_α and D_γ started out low, which are consistent with the aerosol initially containing only a small number of species, both on a per-particle level and on a population level (see Table 1). Over the course of the simulation, both D_α and D_γ increased, but at different rates, which led to changes in χ that we can interpret as changes in mixing state. The initial decrease in χ to about 50% was caused by the emission of fresh combustion particles, containing BC and POA. These emissions continued for the first 12 h of simulation, but at the same time, coagulation and secondary aerosol formation occurred, which (at least initially) efficiently increased the average per-particle diversity D_α. Overall, this led to a more internally mixed population with χ increasing to 72% at 10 h. After this, dilution became relatively more important, introducing background particles, and ammonium nitrate evaporated almost entirely toward the end of the simulation. These combined processes resulted in a slow decrease in χ to 64% at the end of simulation.

The corresponding figure for the low-emission case is shown as Figure S1 in the Supporting Information S1. As expected, for this case, the aerosol number and mass concentrations and the gas-phase concentrations were reduced compared to the high-emission case. For example, the maximum aerosol number concentration at $t = 12$ h only reached to about 1000 cm^{-3} and the maximum SO_2 mixing ratio was only 1.2 ppb. The mixing state metrics (Figure S1d in the Supporting Information S1) ranged between 40% and 78%.

3.2. Aerosol Composition Changes During Cloud Processing

As described in Section 3.1, for each hourly output from the urban plume simulations, cloud cycles were simulated using the same temperature profile shown in Figure 1b. Each cloud parcel simulation was exposed to the same cooling rate but differed in their initial conditions of aerosol populations and gas-phase concentrations. Figure 3 compiles the initial conditions of selected gas-phase species for the cloud parcel simulations using the high-emission case. Each color marks a specific cloud parcel case, which corresponds to a specific plume time t_u. The ranges were consistent with conditions found in polluted urban regions, such as Haikou in southern China with annual average mixing ratios of 2 ppb SO_2 and 7 ppb NO_2 (Wang et al., 2014) and Kanpur in Northern India with annual average mixing ratios of 3 ppb SO_2 and 5.7 ppb NO_2 (Gaur et al., 2014). In this section, we first illustrate the compositional changes during cloud processing, using the aerosol population from the high-emission case at $t_u = 12$ h as the initial conditions for the cloud parcel simulation and focus on the first cloud cycle ($N_{cycle} = 1$).

Figure 4a shows the evolution of several key variables for this case. The initial RH for each cloud parcel simulation was 99%, and the aerosol water content of each particle was adjusted for RH=99% based on the dry aerosol composition. The parcel reached supersaturation within 1 min. During the first 10 min, the liquid water content increased and reached a maximum of 1.23 g kg^{-1} at 10 min. We determined the cloud droplet number concentration following the strategy used in Ching et al. (2012), where particles with wet diameter larger than 2 μm were classified as cloud droplets. As shown in the figure, the cloud droplet number concentration (CDNC) was 2011 cm^{-3} at the time when the maximum supersaturation was reached. This number concentration decreased somewhat as the relative humidity slowly relaxed to saturation, which can be explained by the so-called "inertial effect" (Chuang et al., 1997; Nenes et al., 2001). This refers to droplets with a diameter larger than 2 μm that were not truly activated, i.e., they had a critical diameter larger than 2 μm and this critical diameter was not reached

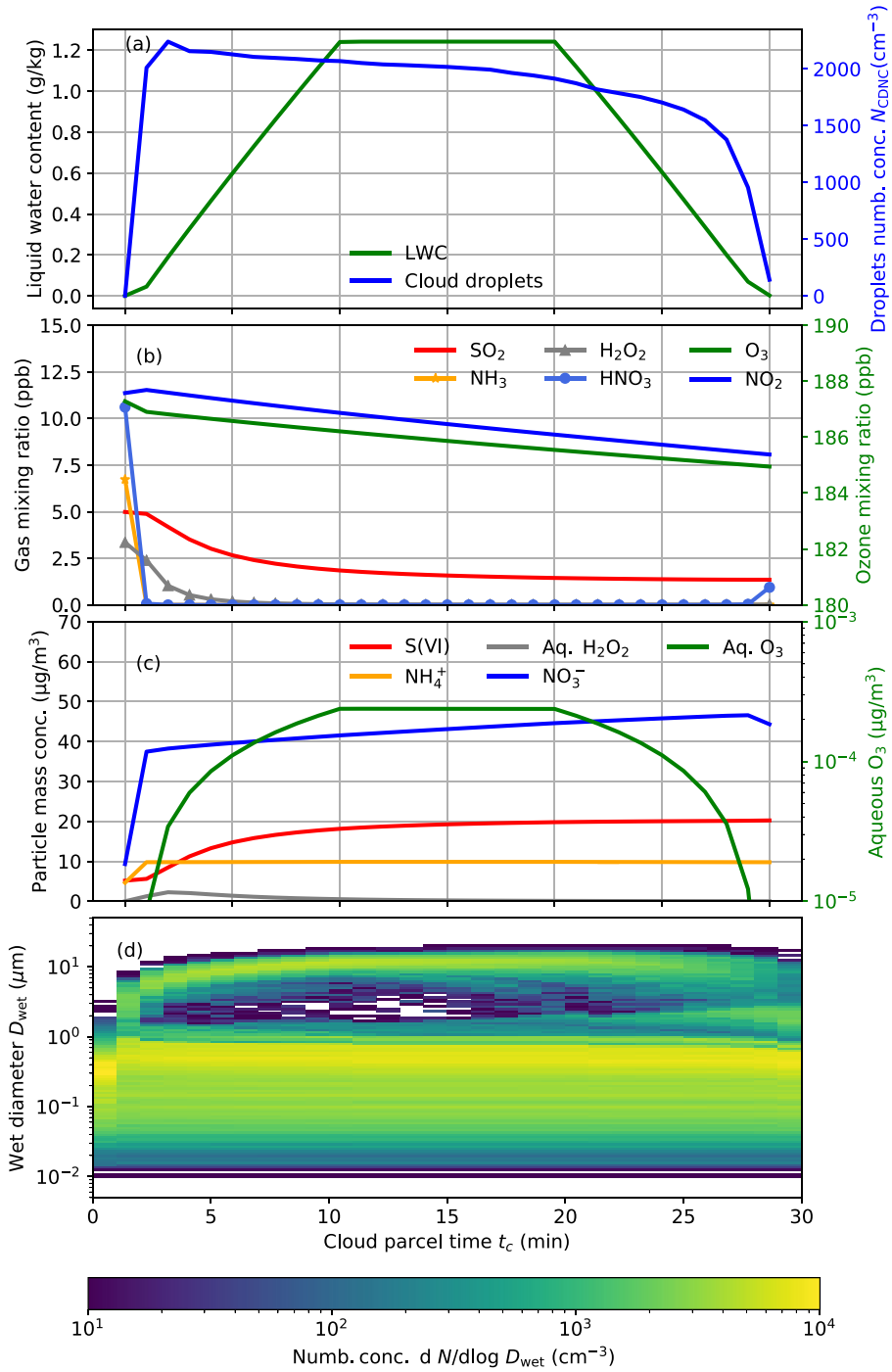


Figure 4. The evolution of (a) liquid water content (LWC) and cloud droplet number concentration (b) mixing ratios of key gas-phase species, (c) key aqueous-phase species, and (d) number concentration with respect to wet diameter. Results are for the aerosol population at t_u = 12 h (high-emission case) and for N_{cycle} = 1.

during the simulation time. After 20 min, as the RH dropped below 100%, the cloud droplet number concentration declined faster and the cloud evaporated.

The CDNC is comparatively high for the example shown in Figure 4, since we started out with a large aerosol number concentration of over 15,000 cm^{-3}. CDNC of this magnitude was observed, for example, during the IMPACT field campaign (Brenguier et al., 2011). Using aerosols from other plume hours as inputs yielded CDNC

below 2000 cm^{-3} as shown in Figure S5 (but always larger than 1000 cm^{-3}). For the low-emission case, the CDNC was much lower, between 100 and 640 cm^{-3}, consistent with observations in more moderately polluted urban environments (Ahmad et al., 2013).

Figure 4b and Figure 4c show the evolution of several key gas and aqueous-phase species. Ammonia in the gas-phase dissolved and immediately formed ammonium. Aqueous-phase NH_4^+ increased from 4.7 to 9.8 μg m^{-3}. Nitrate increased rapidly from 9.3 to 37.4 μg m^{-3} at the beginning due to the uptake of HNO_3. These processes are explained by the R1-R10 reactions in Table S1 in the Supporting Information S1. After this, nitrate was further formed through reaction R15.

The dissolved sulfur dioxide formed SO_3^{2-} and HSO_3^- and could be oxidized to sulfate by aqueous-phase H_2O_2 or O_3 through R11-R15. The sulfate aqueous formation rates are highly pH dependent, and the H_2O_2 oxidation reaction R13 is dominant for pH lower than 5, while the O_3 pathway R12 becomes more important for pH higher than 6 (Seinfeld & Pandis, 2006; Shao et al., 2019). For the cases shown here, the cloud droplets were acidic, and therefore, the oxidation by H_2O_2 dominated. Sulfur dioxide in the gas phase decreased from 4.98 to 1.94 ppb, and the S(VI), including SO_4^{2-} and HSO_4^-, increased from 5.16 to 20.23 μg m^{-3} during the simulation period.

The evolution of the number size distributions based on wet diameter is illustrated in Figure 4d. At $t_c = 0$, the size distribution peaked at 0.3 μm. As discussed above, in less than 1 min, a subset of the particles activated to form cloud droplets and the particle size distribution evolved from initially unimodal to bimodal, with the first peak representing the interstitial (not activated) particles and the second peak representing the cloud droplets. The interstitial aerosol remained unchanged since this simulation did not include coagulation. We will investigate the impact of coagulation further in Section 3.4. With increasing liquid water content and aqueous chemistry processes occurring, the cloud droplets continued to grow and the droplet mode peaked at 11 μm at 20 min.

Next, we will turn to the changes in aerosol-size distributions. To provide a summary of the 25 individual cloud parcel simulations, we show here the average over all 25 scenarios with the variability among cases indicated by the standard deviation (colored band). Figure 5 shows the number and mass concentration as a function of dry diameter before entering the cloud and after each cloud cycle for the high-emission case. After the first cloud cycle, a second mode appeared for the dry number distribution, transforming the unimodal number distribution that peaked at a dry diameter of 0.1 μm to a bimodal distribution with a second peak at 0.3 μm. For each additional cloud cycle, the peak of the second mode kept moving to larger diameters and reached 0.5 μm after the fourth cloud cycle.

The number size distribution of the cloud droplet residuals peaked at a dry diameter of 0.3 μm after the first cloud cycle, which is consistent with field observations (Fast et al., 2019; Ditas et al., 2012; Ge et al., 2012). For subsequent cloud cycles, the diameters increased further, because each cycle added more secondary aerosol mass on the already cloud-processed particles. This may not be representative for real clouds, where particle growth may be limited by gas precursors or oxidants and where entrainment occurs. However, cloud droplet residuals as large as 1 μm aerodynamic diameter were observed for particles collected at a mountain site in Southern China (Lin et al., 2017).

In order to quantify the diameter changes, we define the mean diameter $\bar{D}$ as

$$\bar{D} = \frac{\sum_{i=1}^{n} N_i D_i}{N_{\text{total}}}, \tag{5}$$

where i is the particle index, n is the total number of computational particles, N_{total} is the total number concentration, N_i and D_i are the number concentration and diameter of computation particle i, respectively. The increase in diameter was largest for the first cycle, where $\bar{D}$ increased 24% and grew from 0.1 to 0.124 μm. The fourth cycle only led to a 5% mean diameter increase. For the mass, as shown in Figure 5b, distributions are dominated by the larger particles, as expected. Similar to the trend seen in the number size distribution, the mass increased most in the first cycle. The dry mass concentration, averaged over all 25 cases, increased from 21.2 to 67.2 μg cm^{-3} in the first cycle, which corresponds to 217%. After the fourth cycle, the mass increased from 110.4 to 152.8 μg cm^{-3} (38%).

The size distributions for the low-emission case are shown in Figure S2. The average mode diameter of the cloud droplet mode after the first cycle is somewhat larger (~ 0.35 μm) than in the high-emission case even though the

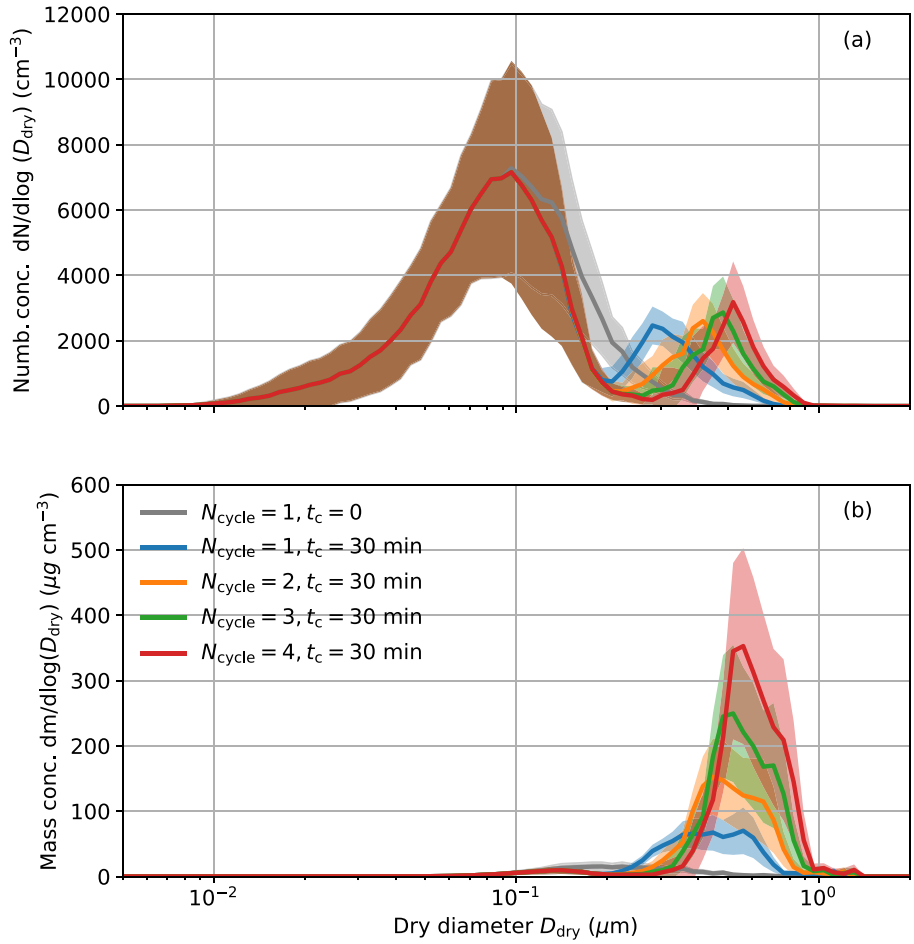


Figure 5. (a) Number and (b) mass size distribution with respect to dry diameter before the first cloud cycle and after each subsequent cloud cycle (high-emission case). The solid lines are the averaged distributions of all 25 cases for each cloud cycle. The shaded area represents the 1σ region of the average. The gray line is the distribution at $t_c = 0$ min, and the other lines are the distributions at the end of each cloud cycle. The composition of the particles was evaluated at RH = 99%. The brown shading in (a) is due to the overlapping colors of different cycles.

gas-phase precursor concentrations were lower. This can be explained by the fact that the CDNC was substantially lower than in the high-emission case, and the gas-phase concentrations were still high enough to allow more secondary aerosol mass to form per droplet.

Figure 6 shows the size-resolved mass fractions averaged over the 25 cases for each cloud simulation at the beginning of the first cloud cycle (gray) and at the end of the fourth cloud cycle (RH = 99%) in high-emission cases. As expected, no change in the size-resolved composition occurred for particles smaller than about 0.1 μm, as these particles remained interstitial aerosol. For the activated particles, the sulfate mass fraction increased from 9.6% to 38.7% in the size range of 0.14–0.25 μm, and the nitrate mass fraction increased from 2.8% to 56.8% in the size range of 0.21–0.89 μm. Ge et al. (2012) also found that particles were more enriched with nitrate and sulfate after aqueous processing from samples collected from the Central Valley of California. For the particles in size range of 0.1–0.2 μm, the fraction of inorganic and SOA species decreased and the fraction of POA and BC species increased after cloud processing. This can be explained by the fact that there were two groups of particles in this size range, one group with mainly inorganic species and SOA and the other group with mainly BC and POA. Particles in the first group were activated and grew larger due to cloud processing. Because more ammonium sulfate and nitrate were produced than SOA, the fraction of inorganics increased more than the SOA fraction. As a result, in the size range of 0.7–0.9 μm, particles transferred from organics dominant to inorganics dominant. The reduced SOA mass fraction in this size range can also be explained by the simplified aqueous SOA formation mechanism in the current study, which for example does not include the formation of IEPOX-derived organosulfates that

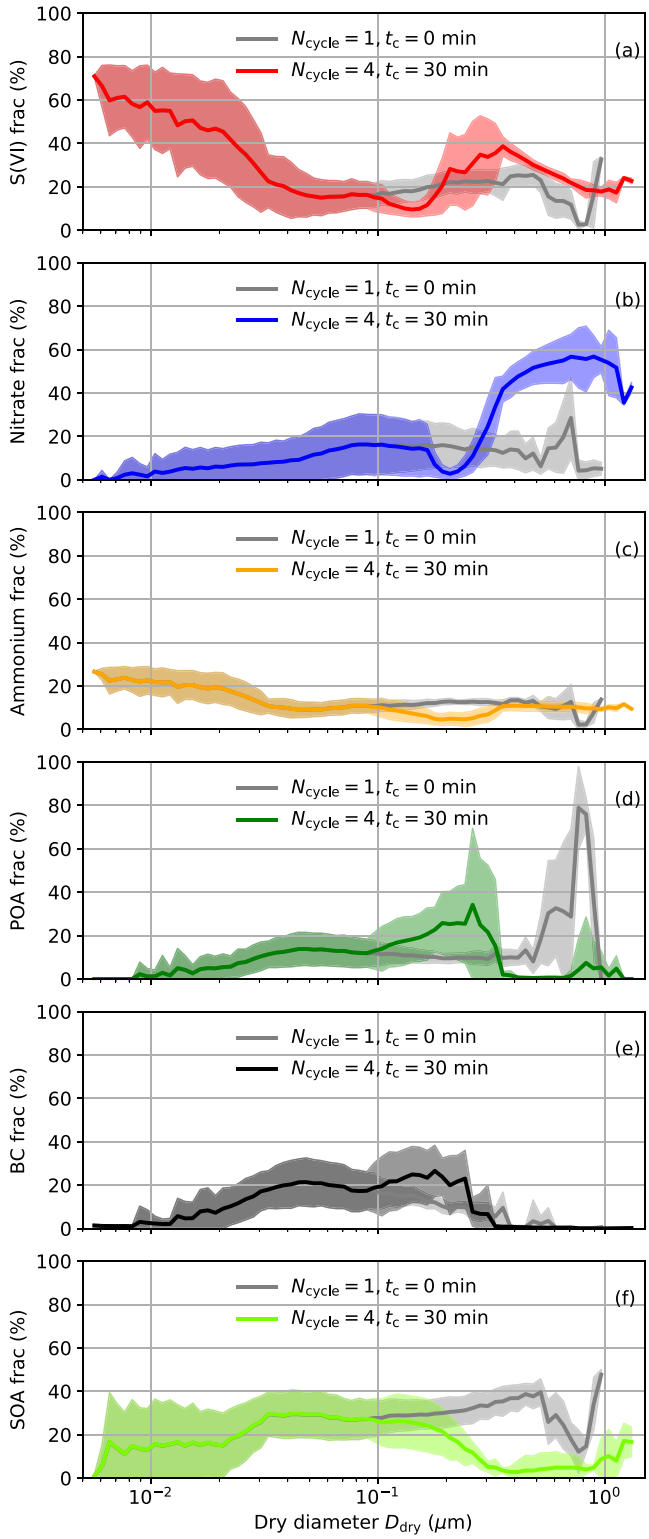


Figure 6. Size-resolved mass fractions of (a) S(VI), (b) nitrate, (c) ammonium, (d) POA, (e) BC, and (f) SOA at $t_c = 0$ min of the first cloud cycle (gray lines), and $t_c = 30$ min after the fourth cloud cycle (colored lines) for the high-emission case. Solid lines are the average values of all 25 cases for each cycle and the shaded band represents the range of one standard deviation. The composition was evaluated at RH = 99%.

have shown to be important in the ambient atmosphere (Hatch et al., 2011). In summary, even in the same size ranges (here 0.1–0.2 μm), particles with different compositions can evolve differently. This is challenging to resolve for models that represent composition with one-dimensional distributions, assuming internally mixed particles within one size bin, and further work is needed to investigate the bias that may be introduced by this assumption.

For our current work, the cloud simulations were set up using the temperature profile shown in figure 1b. Specifically, we considered a cloud that was maintained for about 30 min. In the real environment, clouds may last from minutes to days, depending on cloud type and the surrounding environment (Cotton et al., 2010), and they may also experience a range of different updraft velocities. Since the largest rate of secondary mass formation occurred within a few minutes after the cloud formed, shortening the cloud parcel time did not impact the conclusions as long as the first few minutes were captured. With longer cloud lifetime, secondary aerosol mass formation may continue, provided that the reactants are not depleted. Variations in updraft velocities/cooling rates will result in different maximum supersaturations and hence differences in the subpopulations of activated particles. We did not explore these sensitivities here to keep the scope focused on the changes of particle populations after typical but complete cloud processes.

The previous analyses showed the size-resolved state of the aerosol. However, even within a certain size range, particles can exhibit differences in composition, and we introduced this earlier as the aerosol mixing state. With our particle-resolved modeling approach, we are able to resolve this detail and quantify how aerosol mixing state changes with cloud processing. In order to visualize the change in aerosol mixing state, Figure 7 displays the two-dimensional size distribution of sulfate mass fraction $n(D_{dry}, w_{SO_4})$ for the example of two plume hours $t_u = 0$ and $t_u = 12$ h, before entering the cloud simulation and after four cloud cycles. At the beginning of the urban plume simulation ($t_u = 0$ min), all particles had the same composition and $n(D_{dry}, w_{SO_4})$ was 36% across the entire population (Figure 7a). Over the course of the urban plume simulation, $n(D_{dry}, w_{SO_4})$ was controlled by condensation, coagulation, and dilution processes, and it became more diverse as shown in Figure 7b. The aerosol primary emissions consisted of BC- and POA-containing particles (from gasoline, diesel, and cooking emissions), which over time became coated with sulfate (as well as nitrate and SOA), resulting in particles with sulfate mass fraction of about 20% or less. In Figure 7b, particles in the size range of 0.01–0.2 μm appeared with a sulfate mass fraction of 70%. These are background particles that were introduced into the simulation by dilution with their initial SOA content (model species API1) having evaporated. The low particle number concentrations in between these main particle types originate from coagulation events.

Figure 7c and Figure 7d show the distributions after four cloud cycles. Note that the initial concentrations of the gas-phase species between the two plume hours differed as shown in Figure 2c. Using the population at $t_u = 0$ h, all particles started with the same composition, and particles with diameters larger than 0.1 μm underwent cloud processing, resulting in sulfate mass fractions between 30 and 60%. Since we started with particles that were all identical and after cloud processing, the particles differ in sulfate mass fractions (and other secondary species), the aerosol population became more diverse and more externally mixed. The gap in the 0.1–0.3 μm diameter range was caused by the growth of the activated particles, while the nonactivated particles

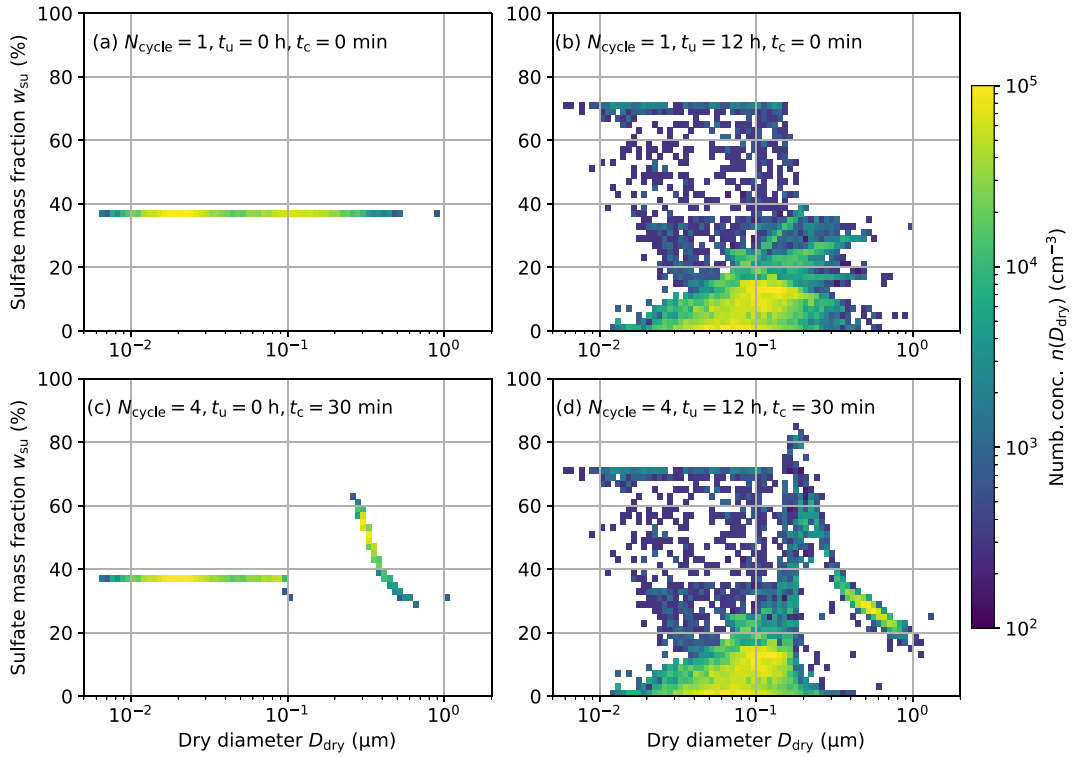


Figure 7. Two-dimensional number concentration distribution $n(D_p, w_{SO4})$ before cloud processing for (a) $t_u = 0$ h and (b) $t_u = 12$ h (high-emission case), (c) population from (a) after four cloud cycles, and (d) population from (b) after four cloud cycles.

remained unchanged. Using the population at $t_u = 12$ h, we can still see the signature of the particles that underwent cloud processing; however, it is difficult to infer if the population became more internally or externally mixed. This is where calculating mixing state metrics will help, which we will investigate next.

3.3. Impacts on Mixing State and Cloud Condensation Nuclei Concentration

As shown qualitatively in Figure 7, cloud processes can change the diversity and the mixing state of particle populations. In this section, we will quantify these changes for our cases more precisely using the metrics described in Section 2.4. Figure 8 shows the evolution of D_α, D_γ and χ after each of the four cloud cycles. After the first

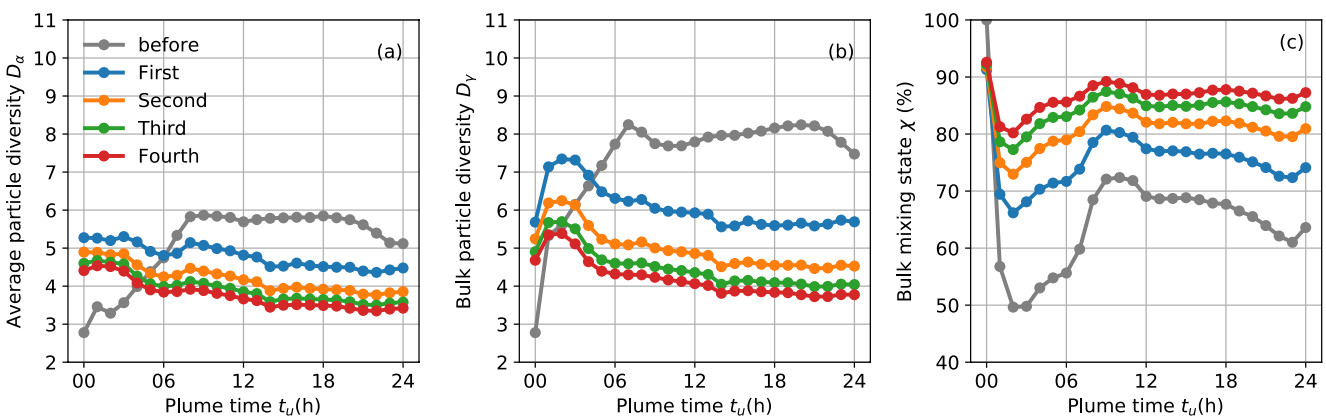


Figure 8. Evolution of (a) average particle diversity D_α, (b) bulk particle diversity D_γ, and (c) bulk mixing state χ (%) at the beginning of cloud cycle 1 and after each of the four cloud cycles (high-emission case).

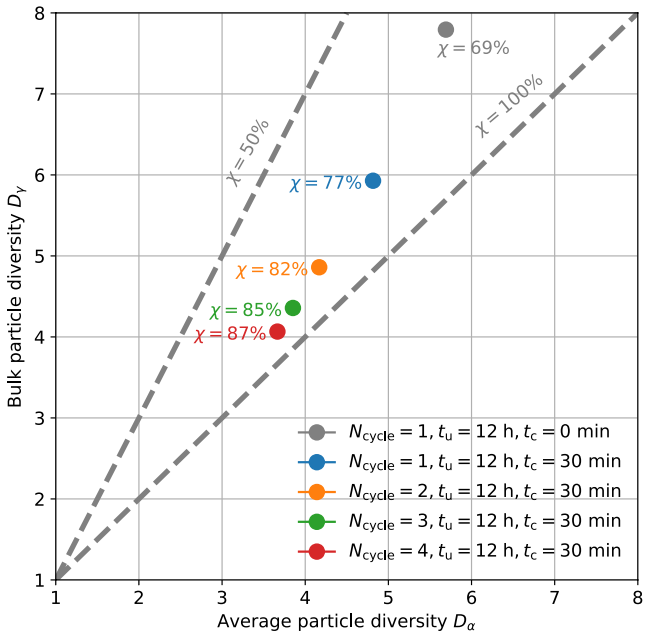


Figure 9. Average particle diversity D_α and bulk particle diversity D_γ diagram for the aerosol at $t_u = 12$ h at the beginning of cloud cycle 1 and after each of the four cloud cycles (high-emission case).

cloud cycle, the average particle species diversity D_α increased for aerosols that used plume hours 0 to 6 as inputs for the cloud parcel simulations. These populations started with relatively low average particle diversities. In contrast, D_α decreased for aerosols that used plume hours 7 to 24 as inputs for the cloud parcel simulations. This illustrates the fact that the addition of aerosol mass (mainly sulfate and nitrate) to a subset of particles in a population can lead to a decrease or increase in average particle diversity, depending on what the starting point is. When D_α was initially low, then adding secondary species led to more diverse particles and D_α increased. This was the case when the aerosol consisted of different types of freshly emitted aerosol and the particles each contained only few species in the early stages of the urban plume simulation. When D_α was initially high, adding a small number of secondary species decreased the diversity, since those newly added species dominated. This was the case when the aerosol consisted of aged particles where several species commonly existed within one particle. This argument applies to both D_α and D_γ. Note that these two cases were contrasted in Riemer and West (2013) as "Prototypical cases 5 and 6." Comparing the different cloud cycles, we observed that each cloud cycle led to a less diverse population than the previous cloud cycle.

If D_α and D_γ changed at the same rate, then χ would remain unchanged by cloud processing. However, here D_α generally decreased less than D_γ, and therefore, χ increased for each cloud parcel simulation. The freshly emitted particles experienced the largest changes, especially for urban plume particle populations at $t_u = 2$ h with χ increasing from 50% to 83% after four cycles. One exception was the case using the aerosol at $t_u = 0$ h as input, which was 100% internally mixed. The first cloud cycle therefore led to a more external mixture (but subsequent cloud cycles led to more internal mixtures); however, this case is likely not relevant for real atmospheric conditions as a completely internal mixture is an idealized assumption.

Figure 9 graphs the progression of the diversity metrics in a $D_\alpha - D_\gamma$ diagram using the aerosol at $t_u = 12$ h as input as an example. After each cloud cycle, the mixing state index moved closer to the diagonal line, which indicates a complete internal mixture ($\chi = 100\%$), with χ increasing from 69% to 87%. However, a complete internal mixture was never reached because the interstitial aerosol still contributed diversity.

The change of aerosol mixing state is likely related to the fraction of activated particles because only those undergo aqueous-phase chemistry. Figure 10 compares cloud droplet number fraction (number concentration of cloud droplets divided by total aerosol concentration at the start of the cloud parcel simulation) and change in mixing state for the high-emission case and the low-emission case for the first cloud cycle. The cloud droplet fraction varied between 10% and 23% and between 20% and 70% for the high-emission and low-emission cases, respectively (Figure 10a). The change in mixing state was indeed larger for the low-emission case where χ reaches values of over 90% after the first cloud cycle (Figure 10b).

CCN properties are determined by particle size and composition. As illustrated above, the activated particles grew during cloud processing and attained high hygroscopicity because of the added ammonium sulfate and ammonium nitrate. Particles with higher hygroscopicity and larger sizes have smaller critical supersaturation and activate at lower supersaturation level. Aerosol hygroscopicity has been observed to increase significantly because of the increased ammonium sulfate and ammonium nitrate mass fraction after cloud processing (Henning et al., 2014; Christiansen et al., 2020; Saliba et al., 2020).

Figure 11a shows the change of CCN spectrum after each cloud cycle for the high-emission case. As before, the solid lines indicate the average over the 25 urban plume cases and the shaded bands show the range of one standard deviation. For environmental supersaturations larger than 0.15%, the CCN/CN ratio remained unchanged after undergoing cloud processing. For supersaturations lower than 0.15%, the CCN/CN ratio increased with the largest increase occurring after the first cloud cycle. This is expected, since the interstitial aerosol remained

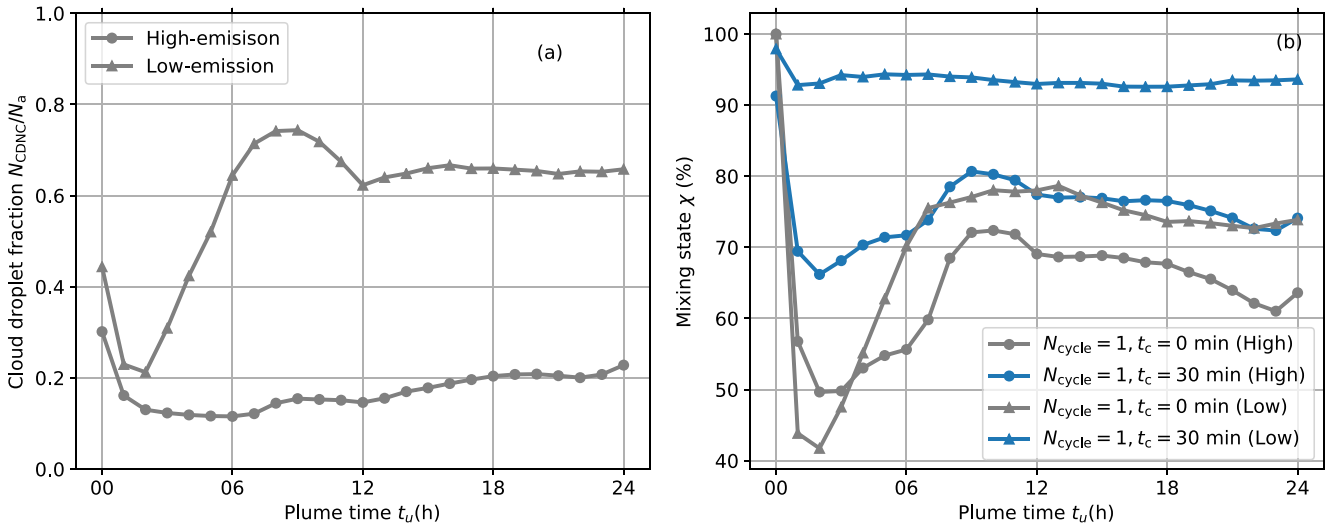


Figure 10. (a) Cloud droplet fraction for the low-emission case and the high-emission case. (b) Mixing state before (gray lines) and after first cloud cycle (blue lines). Circles are for the high-emission case and triangles are for low-emission case.

unchanged during all cloud cycles, and only the particles that formed cloud droplets in the first cycle become progressively more easily activated (i.e., activate at lower and lower supersaturations).

Figure 11b illustrates the changes in CCN number concentration for the individual plume hours and an environmental supersaturation of 0.02%. Before cloud processing, the CCN number concentrations for all plume hours were less than 30 cm^{-3} at this supersaturation level. After cloud processing, the CCN/CN ratio increased to about 12%, which translates to a substantial increase of absolute CCN number concentration because of the large number concentration present in this scenario. For example, the population at t_u = 12 h experienced an increase of CCN concentration from 25 to 547 cm^{-3} after the first cycle. While the CCN concentrations for supersaturations above the value that was reached in the cloud parcel simulations did not change, it was sensitive for supersaturations lower than what was reached in the cloud parcel simulations.

CCN concentrations for supersaturation thresholds larger than 0.15% did not change as a result of aqueous-phase chemistry. This particular threshold value was determined by the maximum supersaturation obtained in our cloud parcel sim-

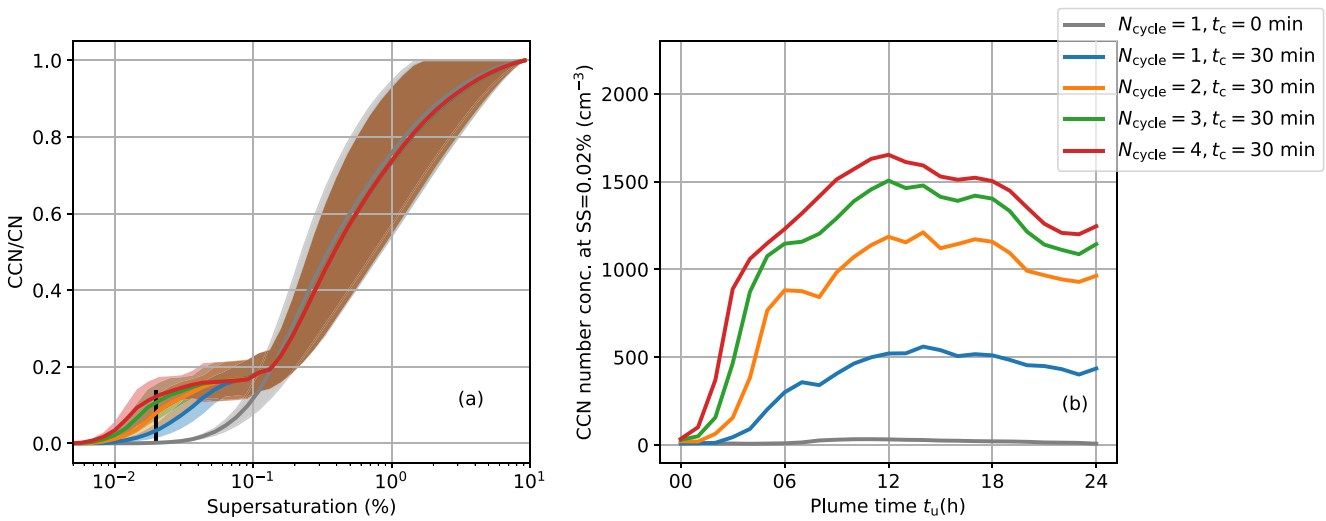


Figure 11. (a) CCN spectrum and (b) CCN number concentration at ss = 0.02% after each of the four cloud cycles (high-emission case). Solid lines in (a) are the mean distributions of all 25 cases at each cycle and the shaded band represents the 1σ range. The black line in (a) indicates the supersaturation level at 0.02%, taken here as an illustrative example.

ulations, which then governs the subpopulation of particles that activate. This threshold value is expected to increase for larger cooling rates, which would result in larger maximum supersaturations (assuming the same aerosol population).

The results look qualitatively similar for the low-emission case (Figure S4 in the Supporting Information S1); however, here the supersaturation threshold above which the CCN/CN did not change was somewhat larger, consistent with the overall higher supersaturations that were reached in the cloud parcel simulations (Figure S5a in the Supporting Information S1).

Increases in CCN/CN ratio are generally attributed to both increased particle size and (potentially) increased hygroscopicity. To disentangle the two factors, we performed a sensitivity calculation where we set the hygroscopicity parameter κ of sulfate, nitrate, and ammonium to 0.1 (representative of SOA) for the particles that had experienced cloud processing (i.e., we artificially decreased the hygroscopicity of these particles). The modified CCN/CN spectrum is shown in Figure S3 in the Supporting Information S1. While the addition of ammonium sulfate and nitrate increased CCN/CN from 0.01 to 0.11 for supersaturations lower than 0.04%, for the sensitivity calculation, the ratio only increased to 0.09. That is, only increasing the size, but keeping κ to a value representative of SOA rather than sulfate or nitrate will reduce the effect by 18%.

It is worth mentioning that our conclusion that CCN concentration increased after cloud processing is based on the changes of critical supersaturation. Previous studies showed that cloud processing can lead in fact to lower cloud droplet number concentrations in subsequent cloud cycles. While an increase in particle size due to aqueous-phase chemistry lowers the critical supersaturation of these particles, their activation and subsequent growth will suppress the environmental supersaturation in the subsequent cloud cycle, overall reducing cloud droplet number concentration (Choularton et al., 1997; Feingold & Kreidenweis, 2000; Romakkaniemi et al., 2006; Ivanova & Leighton, 2008; Bower et al., 1999). In our study, the maximum environmental supersaturation indeed decreased in the following cycles because of the presence of the larger, cloud-processed particles (Figure S5a in the Supporting Information S1), and the cloud droplet concentrations accordingly decrease in the following cycles (Figure S5b in the Supporting Information S1). This is consistent with Feingold and Kreidenweis (2000), where decreased cloud droplet number concentration in the subsequent cloud cycles was found for the environments with an updraft velocity larger than 0.1 m s^{-1} and does not contradict our current findings that processed particles have a higher activation potential.

3.4. Effects of In-Cloud Coagulation on Aerosol Mixing State

So far we presented results that did not account for coagulation events within the cloud. We generally include two different coagulation mechanisms in PartMC, coagulation due to gravitational differential settling using the coagulation efficiencies according to Hall (1980), and Brownian coagulation (Jacobson, 2005). For the size ranges of droplets in our cloud parcel simulations, which is lower than 20 μm and not large enough to initiate effective collision-coalescence (Pruppacher & Klett, 2010), coagulation due to gravitational differential settling was negligible, and therefore, we focus the discussion on the impact of Brownian coagulation. This is a process that is often ignored in aerosol models (Pierce et al., 2015). Pierce et al. (2015) report that interstitial coagulation in clouds led to a 15%–21% decrease of total number concentration globally, associated with a global mean aerosol indirect effect of including interstitial scavenging of +0.5 to +1.3 W m^{-2}.

We use the aerosol from t_u = 12 h as input, since this population had the largest total number concentration (see Figure 2a), and so we expected the impacts of Brownian coagulation to be maximized for this case. Because coagulation events were simulated stochastically and introduce an element of randomness into our simulations, we repeated the cloud parcel simulation three times and reported the average and 95% confidence interval.

Figure 12a compares the number distribution before and after the first cloud cycle including only aqueous chemistry and including aqueous chemistry and coagulation. For the case without Brownian coagulation, the size distribution did not change for diameters smaller than 0.1 μm. With Brownian coagulation, the number concentration of particles smaller than 0.1 μm decreased slightly. The changes in number size distributions comparing t_c = *0* min and 30 min are shown in Figure 12b. Brownian coagulation rates were higher for particle pairs with large diameter difference. Here, Brownian coagulation depleted the number concentration of particles between 0.01−0.1 μm (the interstitial aerosol). The effects of aqueous-phase chemistry occurred at larger sizes and moved the particles from 0.1−0.3 μm to 0.3−0.5 μm.

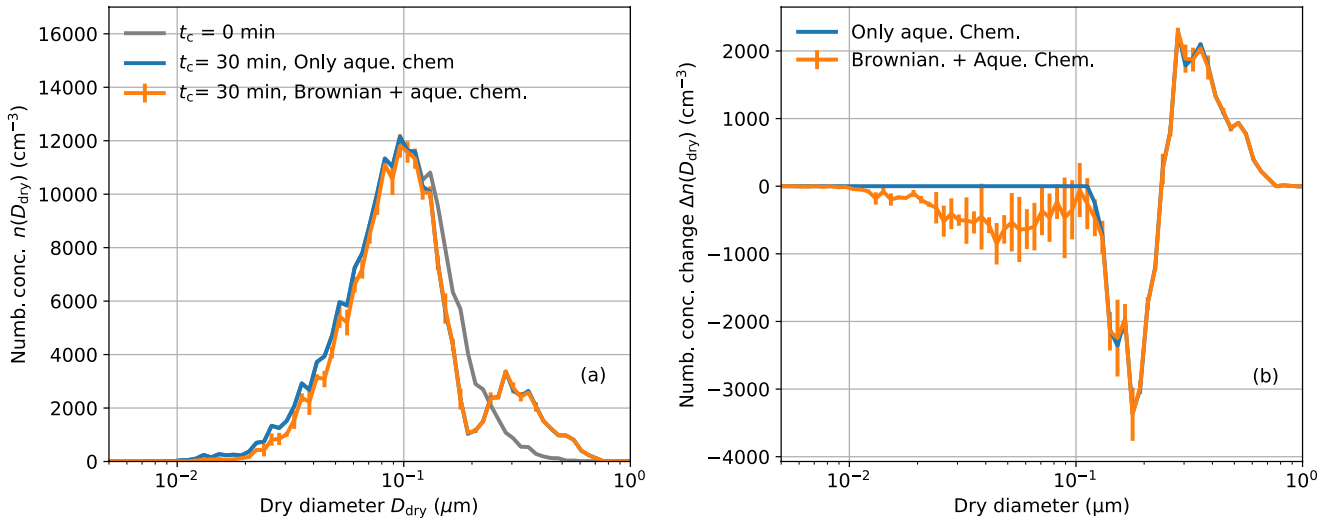


Figure 12. (a) Number distribution at initial condition $t_c = 0$ (gray), at $t_c = 30$ min with aqueous chemistry only (blue) and at $t_c = 30$ min with Brownian coagulation and aqueous chemistry (orange); (b) the change of number size distribution due to aqueous chemistry and Brownian coagulation. The solid orange line is the average of three realizations of the cloud parcel model simulation and the error bar is the 95% confidence interval.

Since Brownian coagulation in the cloud mainly affected interstitial particles, the changes to the CCN spectrum were expected to be small and should be mainly visible for higher supersaturation levels. As shown in Figure 13, the CCN spectrum moved left only for supersaturation level higher than 0.2%. For example, with Brownian coagulation, the CCN/CN ratio increased by 4.1% from 0.74 to 0.77 at ss = 0.5 %. Figure 13b shows the change of CN (total aerosol number concentrations) and CCN concentrations in the simulated 30 minutes. Since the decrease of total aerosol concentration was larger, this led to the reported increase in CCN/CN ratio. Including Brownian coagulation caused a decrease of total aerosol concentration (by 5.9%) and of CCN concentration (by 1.7%) over the 30-min cloud parcel simulation. We expect this effect to be more pronounced for aerosol populations that contain a nucleation mode (Romakkaniemi et al., 2006), which our case did not include.

Figure 13c shows the evolution of D_α and D_γ using output from every minute during the cloud parcel simulation. The trajectory of the case with Brownian coagulation was almost identical with the case without Brownian coagulation, indicating negligible effects of coagulation on mixing state. Although the differences were small, it was noticeable that including coagulation does not change D_γ, since the aerosol bulk mass concentrations were not changed. However, it increased D_α, since the average particle diversity increases during coagulation (archetypical Case 4 in Riemer and West (2013)).

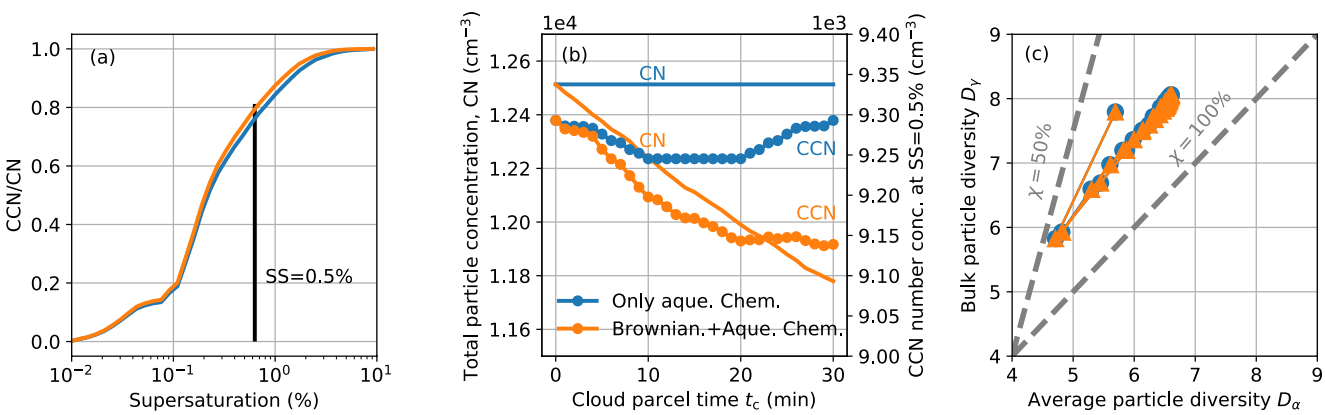


Figure 13. (a) CCN spectrum and (b) total CN and CCN concentration at ss = 0.5% with only aqueous chemistry (blue) and with both Brownian coagulation and aqueous chemistry (orange). The vertical line in (a) is for ss = 0.5%, and solid and dotted lines in (b) are for total CN and CCN concentrations at that level, respectively. (c) Effects of coagulation on aerosol mixing state metrics. The points correspond to output from every minute during the cloud parcel simulation.

4. Conclusions

In this study, we investigated the impact of in-cloud aqueous-phase chemistry on aerosol mixing state. Using the particle-resolved model PartMC-MOSAIC, we generated particle populations of different aerosol mixing states from urban plume simulations representing polluted conditions. We used these as inputs for 30-min cloud parcel simulations that included the reduced CAPRAM 2.4 aqueous-phase chemistry mechanism. Each cloud parcel simulation was driven by the same temperature profile, with decreasing temperature during the first 10 min, constant temperature during the second 10 min, and increasing temperature during the third 10 min. While the cloud parcel simulations were simplified in that we assumed adiabatic conditions, our results are a first step toward investigating aerosol-cloud interactions within a particle-resolved framework that allows for representing aerosol mixing state without simplifying assumptions.

Coming back to the questions that we posed in the introduction, we conclude the following. We quantified changes in mixing state as a result of in-cloud processes using the diversity metrics D_α (average particle diversity) and D_γ (bulk aerosol diversity) and the mixing state index χ. The aqueous-phase chemistry processes had an "equalizing effect" on the diversity metrics, meaning that D_α and D_γ increased due to aqueous-phase chemistry when the initial values were low and decreased when the initial values were high. The first condition applied for plume time hours 0–6 in our high-emission scenario, when fresh emissions dominated which tend to be of low diversity, consistent with observational findings (Healy et al., 2014). Adding secondary species to the activated particles increased the diversities. The opposite was the case when D_α and D_γ values started out high, which applied to plume time hours 7–24, when the plume was aged. Here, adding secondary species to the activated particles decreased the diversities.

Whether the overall population became more or less internally mixed depended on the relative changes in D_α and D_γ. For most populations in our study, aqueous-phase chemistry led to a more internally mixed aerosol. For example, for the population of plume hour $t_u = 12$ h, χ increased from 69% to 77% after the first cloud cycle, and to 87% after the fourth cloud cycle. However, a completely internal mixture was not achieved under the conditions investigated here, since only a portion of the aerosol population activated and the remaining interstitial aerosol always contributed diversity to the population. An exception was the case of plume hour $t_u = 0$, when the initial aerosol population was completely internally mixed. In this case, aqueous-phase chemistry caused the population to become more externally mixed.

The change in mixing state index χ due to cloud processing depended also on the fraction of particles that formed cloud droplets. In our high-emission case, this fraction remained below 23% and χ did not exceed 90% even after the fourth cloud cycle. In contrast, for the low-emission case, the fraction of activated particles ranged between 20% and 75%, and χ increased to over 90% after the first cloud cycle.

The size changes after cloud processing led to significant changes to aerosol microphysical properties. With ammonium nitrate and ammonium sulfate added to the activated particles, after the cloud evaporated, the activation potential of the resuspended aerosol particles increased remarkably for low supersaturation thresholds. For example, the CCN concentration for particles from the high-emission case at $t_u = 12$ h, and supersaturation level 0.02% increased by a factor of 20 from 30 cm^{-3} to 547 cm^{-3} after the first cloud cycle. For subsequent cloud cycles, the increase was smaller and by the fourth cycle, it was only 8.8%.

The effects of coagulation due to gravitational settling were negligible in our simulations. This can be explained by the fact that the cloud droplets did not grow large enough for gravitational settling to take over as main coagulation mechanisms. Brownian coagulation occurred mainly between the interstitial particles at around 0.1 μm and cloud droplets at 10 μm. The number concentration reduction caused by coagulation was up to 5.8 % in the cases considered, while the CCN concentration was reduced by less than 2%. This therefore resulted in an increase of the CCN/CN ratio for supersaturations higher than 0.2%. The change in aerosol mixing state caused by coagulation was negligible. It should be noted that our simulations did not take into account the impact of phoretic or turbulence effects on coagulation, which could modify the efficiency of in-cloud coagulation.

Data Availability Statement

The simulation data of the particle-resolved modeling are available at: https://doi.org/10.13012/B2IDB-8367769%5FV1.

Acknowledgments
Yu Yao, Nicole Riemer, and Matthew L. Dawson acknowledge funding from the National Science Foundation, Atmospheric and Geospace Sciences NSF AGS CAREER grant 1254428. This publication was also developed under Assistance Agreement no. EPA 83588101 awarded by the US Environmental Protection Agency to the Regents of the University of California. It has not been formally reviewed by the EPA. The views expressed in this document are solely those of the authors and do not necessarily reflect those of the agency. The EPA does not endorse any products or commercial services mentioned in this publication.

References

Ahmad, I., Mielonen, T., Grosvenor, D. P., Portin, H. J., Arola, A., Mikkonen, S., et al. (2013). Long-term measurements of cloud droplet concentrations and aerosol–cloud interactions in continental boundary layer clouds. *Tellus B: Chemical and Physical Meteorology*, *65*(1), 20138. https://doi.org/10.3402/tellusb.v65i0.20138

Alexander, B., Park, R. J., Jacob, D. J., & Gong, S. (2009). Transition metal-catalyzed oxidation of atmospheric sulfur: Global implications for the sulfur budget. *Journal of Geophysical Research: Atmospheres*, *114*(2), 1–13. https://doi.org/10.1029/2008JD010486

Andrejczuk, M., Reisner, J., Henson, B., Dubey, M., & Jeffry, C. (2008). The potential impacts of pollution on a nondrizzling stratus deck: Does aerosol number matter more than type? *Journal of Geophysical Research: Atmospheres*, *113*, D19204. https://doi.org/10.1029/2007JD009445

Barth, M. C. (2006). The importance of cloud drop representation on cloud photochemistry. *Atmospheric Research*, *82*(1-2), 294–309. https://doi.org/10.1016/j.atmosres.2005.10.008

Barth, M. C., Sillman, S., Hudman, R., Jacobson, M. Z., Kim, C. H., Monod, A., & Liang, J. (2003). Summary of the cloud chemistry modeling intercomparison: Photochemical box model simulation. *Journal of Geophysical Research: Atmospheres*, *108*(7). https://doi.org/10.1029/2002jd002673

Bauer, S., Wright, D., Koch, D., Lewis, E., McGraw, R., Chang, L.-S., & Ruedy, R. (2008). MATRIX (Multiconfiguration Aerosol TRacker of mIXing state): An aerosol microphysical module for global atmospheric models. *Atmospheric Chemistry and Physics*, *8*(20), 6003–6035. https://doi.org/10.5194/acp-8-6003-2008

Bhattu, D., & Tripathi, S. N. (2015). CCN closure study: Effects of aerosol chemical composition and mixing state. *Journal of Geophysical Research: Atmospheres*, *120*(2), 766–783. https://doi.org/10.1002/2014JD021978

Bondy, A. L., Bonanno, D., Moffet, R. C., Wang, B., Laskin, A., & Ault, A. P. (2018). The diverse chemical mixing state of aerosol particles in the southeastern United States. *Atmospheric Chemistry and Physics*, *18*(16), 12595–12612. https://doi.org/10.5194/acp-18-12595-2018

Bott, A., Trautmann, T., & Zdunkowski, W. (1996). A numerical model of the cloud-topped planetary boundary layer: Radiation, turbulence and spectral microphysics in marine stratus. *Quarterly Journal of the Royal Meteorological Society*, *122*, 635–667. https://doi.org/10.1002/qj.49712253105

Bower, K., Jones, A., & Choularton, T. (1999). A modelling study of aerosol processing by stratocumulus clouds and its impact on general circulation model parameterisations of cloud and aerosol. *Atmospheric Research*, *50*(3-4), 317–344. https://doi.org/10.1016/s0169-8095(98)00100-8

Brenguier, J.-L., Burnet, F., & Geoffroy, O. (2011). Cloud optical thickness and liquid water path–does the *k* coefficient vary with droplet concentration? *Atmospheric Chemistry and Physics*, *11*(18), 9771–9786. https://doi.org/10.5194/acp-11-9771-2011

Broekhuizen, K., Chang, R. Y., Leaitch, W. R., Li, S., & Abbatt, J. P. D. (2006). Closure between measured and modeled cloud condensation nuclei (CCN) using size-resolved aerosol compositions in downtown Toronto. *Atmospheric Chemistry and Physics*, *6*, 2513–2524. https://doi.org/10.5194/acp-6-2513-2006

Ching, J., Adachi, K., Zaizen, Y., Igarashi, Y., & Kajino, M. (2019). Aerosol mixing state revealed by transmission electron microscopy pertaining to cloud formation and human airway deposition. *npj Clim Atmos Sci*, *2*(1), 22. https://doi.org/10.1038/s41612-019-0081-9

Ching, J., Fast, J., West, M., & Riemer, N. (2017). Metrics to quantify the importance of mixing state for CCN activity. *Atmospheric Chemistry and Physics*, *17*, 7445–7458. https://doi.org/10.5194/acp-17-7445-2017

Ching, J., & Kajino, M. (2018). Aerosol mixing state matters for particles deposition in human respiratory system. *Scientific Reports*, *8*(1), 8864. https://doi.org/10.1038/s41598-018-27156-z

Ching, J., Riemer, N., & West, M. (2012). Impacts of black carbon mixing state on black carbon nucleation scavenging: Insights from a particle-resolved model. *Journal of Geophysical Research: Atmospheres*, *117*(23), 1–21. https://doi.org/10.1029/2012JD018269

Ching, J., Riemer, N., & West, M. (2016). Black carbon mixing state impacts on cloud microphysical properties: Effects of aerosol plume and environmental conditions. *Journal of Geophysical Research: Atmospheres*, 5990–6013. https://doi.org/10.1002/2016JD024851

Choularton, T., Bower, K., & Gallagher, M. (1997). The effect of sulphur chemistry on the scattering properties of particles. *Philosophical Transactions of the Royal Society of London. Series B: Biological Sciences*, *352*(1350), 213–220. https://doi.org/10.1098/rstb.1997.0016

Christiansen, A. E., Carlton, A. G., & Henderson, B. H. (2020). Differences in fine particle chemical composition on clear and cloudy days. *Atmospheric Chemistry and Physics*, *20*(19), 11607–11624. https://doi.org/10.5194/acp-20-11607-2020

Chuang, P. Y., Charlson, R. J., & Seinfeld, J. H. (1997). Kinetic limitations on droplet formation in clouds. *Nature*, *390*(6660), 594–596. https://doi.org/10.1038/37576

Cohen, S. D., Hindmarsh, A. C., & Dubois, P. F. (1996). CVODE, A Stiff/Nonstiff ODE Solver in C. *Computers in Physics*, *10*(2). https://doi.org/10.1063/1.4822377

Collett, J., Bator, A., Rao, X., & Demoz, B. B. (1994). Acidity variations across the cloud drop size spectrum and their influence on rates of atmospheric sulfate production. *Geophysical Research Letters*, *21*(22), 2393–2396. https://doi.org/10.1029/94GL02480

Cooper, W., Bruintjes, R., & Mather, G. (1997). Calculations pertaining to hygroscopic seeding with flares. *Journal of Applied Meteorology*, *36*, 1449–1469. https://doi.org/10.1175/1520-0450(1997)036<1449:cpthsw>2.0.co;2

Cotton, W. R., Bryan, G., & Van den Heever, S. C. (2010). *Storm and cloud dynamics*. Academic press.

Crooks, M., Connolly, P., & McFiggans, G. (2018). A parameterisation for the co-condensation of semi-volatile organics into multiple aerosol particle modes. *Geoscientific Model Development*, *11*(8), 3261–3278. https://doi.org/10.5194/gmd-11-3261-2018

Ditas, F., Shaw, R. A., Siebert, H., Simmel, M., Wehner, B., & Wiedensohler, A. (2012). Aerosols-cloud microphysics-thermodynamics-turbulence: Evaluating supersaturation in a marine stratocumulus cloud. *Atmospheric Chemistry and Physics*, *12*(5), 2459–2468. https://doi.org/10.5194/acp-12-2459-2012

Ervens, B. (2015). Modeling the processing of aerosol and trace gases in clouds and fogs. *Chemical Reviews*, *115*(10), 4157–4198. https://doi.org/10.1021/cr5005887

Ervens, B., George, C., Williams, J., Buxton, G., Salmon, G., Bydder, M., et al. (2003). Capram 2.4 (MODAC mechanism): An extended and condensed tropospheric aqueous phase mechanism and its application. *Journal of Geophysical Research: Atmospheres*, *108*(D14). https://doi.org/10.1029/2002jd002202

Fahey, K. M., Carlton, A. G., Pye, H. O., Baek, J., Hutzell, W. T., Stanier, C. O., et al. (2017). A framework for expanding aqueous chemistry in the Community Multiscale Air Quality (CMAQ) model version 5.1. *Geoscientific Model Development*, *10*(4), 1587–1605. https://doi.org/10.5194/gmd-10-1587-2017

Fast, J. D., Berg, L. K., Feng, Z., Mei, F., Newsom, R., Sakaguchi, K., & Xiao, H. (2019). The impact of variable land-atmosphere coupling on convective cloud populations observed during the 2016 HI-SCALE field campaign. *Journal of Advances in Modeling Earth Systems*, *11*(8), 2629–2654. https://doi.org/10.1029/2019ms001727

Feingold, G., & Kreidenweis, S. (2000). Does cloud processing of aerosol enhance droplet concentrations? *Journal of Geophysical Research: Atmospheres*, *105*(D19), 24351–24361. https://doi.org/10.1029/2000jd900369

Feingold, G., Kreidenweis, S. M., Stevens, B., & Cotton, W. (1996). Numerical simulations of stratocumulus processing of cloud condensation nuclei through collision coalescence. *Journal of Geophysical Research: Atmospheres*, *101*, 21391–21402. https://doi.org/10.1029/96jd01552

Fierce, L., Onasch, T. B., Cappa, C. D., Mazzoleni, C., China, S., Bhandari, J., & Wolff, L. (2020). Radiative absorption enhancements by black carbon controlled by particle-to-particle heterogeneity in composition. *Proceedings of the National Academy of Sciences*, *117*(10), 5196–5203. https://doi.org/10.1073/pnas.1919723117

Fierce, L., Riemer, N., & Bond, T. C. (2017). Toward reduced representation of mixing state for simulating aerosol effects on climate. *Bulletin of the American Meteorological Society*, *98*(5), 971–980. https://doi.org/10.1175/BAMS-D-16-0028.1

Flossmann, A. (1994). A 2-D spectral model simulation of the scavenging of gaseous and particulate sulfate by warm marine clouds. *Atmospheric Research*, *32*, 233–248. https://doi.org/10.1016/0169-8095(94)90063-9

Gao, W., Fan, J., Easter, R., Yang, Q., Zhao, C., & Ghan, S. J. (2016). Coupling spectral-bin cloud microphysics with the MOSAIC aerosol model in WRF-Chem: Methodology and results for marine stratocumulus clouds. *Journal of Advances in Modeling Earth Systems*, *8*, 1289–1309. https://doi.org/10.1002/2016ms000676

Gaur, A., Tripathi, S., Kanawade, V., Tare, V., & Shukla, S. (2014). Four-year measurements of trace gases (SO_2, NO_x, CO, and O_3) at an urban location, Kanpur, in northern India. *Journal of Atmospheric Chemistry*, *71*(4), 283–301. https://doi.org/10.1007/s10874-014-9295-8

Ge, X., Zhang, Q., Sun, Y., Ruehl, C. R., & Setyan, A. (2012). Effect of aqueous-phase processing on aerosol chemistry and size distributions in Fresno, California, during wintertime. *Environmental Chemistry*, *9*(3), 221–235. https://doi.org/10.1071/en11168

Grabowski, W. W., Morrison, H., Shima, S.-I., Abade, G. C., Dziekan, P., & Pawlowska, H. (2019). Modeling of cloud microphysics: Can we do better? *Bulletin of the American Meteorological Society*, *100*(4), 655–672. https://doi.org/10.1175/BAMS-D-18-0005.1

Hall, D. W. (1980). A detailed microphysical model within a two-dimensional dynamic framework: Model description and preliminary results. *Journal of the Atmospheric Sciences*, *37*, 2486–2507. https://doi.org/10.1175/1520-0469(1980)037<2486:ADMMWA>2.0.CO;2

Harris, E., Sinha, B., Pinxteren, D. V., Tilgner, A., Fomba, K. W., Schneider, J., et al. (2013). Enhanced role of transition metal oxidation of SO_2. *Science*, *340*(6133), 727–730. https://doi.org/10.1126/science.1230911

Hatch, L. E., Creamean, J. M., Ault, A. P., Surratt, J. D., Chan, M. N., Seinfeld, J. H., et al. (2011). Measurements of isoprene-derived organosulfates in ambient aerosols by aerosol time-of-flight mass spectrometry-Part 1: Single particle atmospheric observations in Atlanta. *Environmental Science & Technology*, *45*(12), 5105–5111. https://doi.org/10.1021/es103944a

Healy, R., Riemer, N., Wenger, J., Murphy, M., West, M., Poulain, L., et al. (2014). Single particle diversity and mixing state measurements. *Atmospheric Chemistry and Physics*, *14*, 6289–6299. https://doi.org/10.5194/acp-14-6289-2014

Hegg, D. A., et al. (1990). The effects of microphysical parameterization on model predictions of sulfate production in clouds. *Tellus B*, *42*(3), 272–284. https://doi.org/10.3402/tellusb.v42i3.15220

Henning, S., Dieckmann, K., Ignatius, K., Schäfer, M., Zedler, P., Harris, E., et al. (2014). Influence of cloud processing on CCN activation behaviour in the Thuringian Forest, Germany during HCCT-2010. *Atmospheric Chemistry and Physics*, *14*(15), 7859–7868. https://doi.org/10.5194/acp-14-7859-2014

Hindmarsh, A. C., Brown, P. N., Grant, K. E., Lee, S. L., Serban, R., Shumaker, D. A. N. E., & Woodward, C. S. (2005). SUNDIALS : Suite of Nonlinear and Differential / Algebraic Equation Solvers. *ACM Transactions on Mathematical Software*, *31*(3), 363–396. https://doi.org/10.1145/1089014.1089020

Hoag, K. J., Collett, J. L., Jr, & Pandis, S. N. (1999). The influence of drop size-dependent fog chemistry on aerosol processing by San Joaquin valley fogs. *Atmospheric Environment*, *33*(29), 4817–4832. https://doi.org/10.1016/S1352-2310(99)00268-X

Hoose, C., Lohmann, U., Bennartz, R., Croft, B., & Lesins, G. (2008). Global simulations of aerosol processing in clouds. *Atmospheric Chemistry and Physics*, *8*(23), 6939–6963. https://doi.org/10.5194/acp-8-6939-2008

Hoppel, W., Frick, G., & Larson, R. (1986). Effect of nonprecipitating clouds on the aerosol size distribution in the marine boundary layer. *Geophysical Research Letters*, *13*(2), 125–128. https://doi.org/10.1029/GL013i002p00125

Ivanova, I. T., & Leighton, H. G. (2008). Aerosol–cloud interactions in a mesoscale model. Part II: Sensitivity to aqueous-phase chemistry. *Journal of Atmospheric Sciences*, *65*(2), 309–330. https://doi.org/10.1175/2007jas2276.1

Jacobson, M. Z. (2001). Strong radiative heating due to the mixing state of black carbon in atmospheric aerosols. *Nature*, *409*(6821), 695–697. https://doi.org/10.1038/35055518

Jacobson, M. Z. (2005). *Fundamentals of atmospheric modeling*. Cambridge University Press.

Jaruga, A., & Pawlowska, H. (2018). libcloudph++2.0: aqueoous-phase chemistry extension of the particle-based cloud microphysics scheme. *Geoscientific Model Development*, *11*, 3623–3645. https://doi.org/10.5194/gmd-11-3623-2018

Knopf, D. A., Alpert, P. A., & Wang, B. (2018). The role of organic aerosol in atmospheric ice nucleation: A review. *ACS Earth Space Chem*, *2*(3), 168–202. https://doi.org/10.1021/acsearthspacechem.7b00120

Kreidenweis, S., Walcek, C., Feingold, G., Gong, W., Jacobson, M., Kim, C.-H., & Seinfeld, J. (2003). Modification of aerosol mass and size distribution due to aqueous phase SO_2 oxidation in clouds: Comparisons of several models. *Journal of Geophysical Research: Atmospheres*, *108*, 8630. https://doi.org/10.1029/2002JD002697

Lance, S., Barth, M., & Carlton, A. (2017). Multiphase chemistry: Experimental design for coordinated measurement and modeling studies of cloud processing at a mountaintop. *Bulletin of the American Meteorological Society*, *98*(7), ES163–ES167. https://doi.org/10.1175/BAMS-D-17-0015.1

Lesins, G., Chylek, P., & Lohmann, U. (2002). A study of internal and external mixing scenarios and its effect on aerosol optical properties and direct radiative forcing. *Journal of Geophysical Research: Atmospheres*, *107*(D10)–12. AAC 5-1-AAC 5. https://doi.org/10.1029/2001JD000973

Li, W., Li, P., Sun, G., Zhou, S., Yuan, Q., & Wang, W. (2011). Cloud residues and interstitial aerosols from non-precipitating clouds over an industrial and urban area in northern China. *Atmospheric Environment*, *45*(15), 2488–2495. https://doi.org/10.1016/j.atmosenv.2011.02.044

Lian, X., Ou, J., Zhang, G., Li, M., Tang, M., Zhou, Z., & Chen, D. (2019). In-cloud formation of secondary species in iron-containing particles. *Atmospheric Chemistry and Physics*, *19*(2), 1195–1206. https://doi.org/10.5194/acp-19-1195-2019

Liggio, J., Gordon, M., Smallwood, G., Li, S.-M., Stroud, C., Staebler, R., et al. (2012). Are emissions of black carbon from gasoline vehicles underestimated? Insights from near and on-road measurements. *Environmental Science & Technology*, *46*(9), 4819–4828. https://doi.org/10.1021/es2033845

Lin, Q., Zhang, G., Peng, L., Bi, X., Wang, X., Brechtel, F. J., et al. (2017). In situ chemical composition measurement of individual cloud residue particles at a mountain site, southern China. *Atmospheric Chemistry and Physics*, *17*(13), 8473–8488. https://doi.org/10.5194/acp-17-8473-2017

Mayol-Bracero, O. L., Gabriel, R., Andreae, M. O., Kirchstetter, T. W., Novakov, T., Ogren, J., et al. (2002). Carbonaceous aerosols over the Indian Ocean during the Indian Ocean Experiment (INDOEX): Chemical characterization, optical properties, and probable sources. *Journal of Geophysical Research: Atmospheres*, *107*(19). https://doi.org/10.1029/2000JD000039

McNeill, V. F. (2015). Aqueous organic chemistry in the atmosphere: Sources and chemical processing of organic aerosols. *Environmental Science and Technology*, *49*(3), 1237–1244. https://doi.org/10.1021/es5043707

Nam, E., Fulper, C., Warily, J., Somers, J., Michaels, H., Baldauf, R., et al. (2008). *Technical Report EPA420-R-08-010* (p. 85). Environmental Protection Agency.

Nenes, A., Ghan, S., Abdul-Razzak, H., Chuang, P. Y., & Seinfeld, J. H. (2001). Kinetic limitations on cloud droplet formation and impact on cloud albedo. *Tellus B: Chemical and Physical Meteorology*, *53*(2), 133–149. https://doi.org/10.3402/tellusb.v53i2.16569

Noble, S. R., & Hudson, J. G. (2019). Effects of continental clouds on surface Aitken and accumulation modes. *Journal of Geophysical Research: Atmospheres*, *124*(10), 5479–5502. https://doi.org/10.1029/2019JD030297

Ovchinnikov, M., & Easter, R. (2010). Modeling aerosol growth by aqueous chemistry in a nonprecipitating cloud. *Journal of Geophysical Research: Atmospheres*, *115*, D14210. https://doi.org/10.1029/2009JD012816

Petters, M. D., & Kreidenweis, S. M. (2007). A single parameter representation of hygroscopic growth and cloud condensation nucleus activity. *Atmospheric Chemistry and Physics*, *7*(8), 1961–1971. https://doi.org/10.5194/acp-7-1961-2007

Pierce, J. R., Croft, B., Kodros, J. K., D'Andrea, S. D., & Martin, R. V. (2015). The importance of interstitial particle scavenging by cloud droplets in shaping the remote aerosol size distribution and global aerosol-climate effects. *Atmospheric Chemistry and Physics*, *15*(11), 6147–6158. https://doi.org/10.5194/acp-15-6147-2015

Pruppacher, H. R., & Klett, J. D. (2010). *Microphysics of clouds and precipitation* (2nd ed.). Springer Science & Business Media.

Pye, H. O., Nenes, A., Alexander, B., Ault, A. P., Barth, M. C., Clegg, S. L., et al. (2020). The acidity of atmospheric particles and clouds. *Atmospheric Chemistry and Physics*, *20*(8), 4809–4888. https://doi.org/10.5194/acp-20-4809-2020

Riemer, N., Ault, A. P., West, M., Craig, R. L., & Curtis, J. H. (2019). Aerosol mixing state: Measurements, modeling, and impacts. *Reviews of Geophysics*, *57*, 187–249. https://doi.org/10.1029/2018RG000615

Riemer, N., Vogel, H., Vogel, B., & Fiedler, F. (2003). Modeling aerosols on the mesoscale-γ: Treatment of soot aerosol and its radiative effects. *Journal of Geophysical Research: Atmospheres*, *108*(D19). https://doi.org/10.1029/2003JD003448

Riemer, N., & West, M. (2013). Quantifying aerosol mixing state with entropy and diversity measures. *Atmospheric Chemistry and Physics*, *13*(22), 11423–11439. https://doi.org/10.5194/acp-13-11423-2013

Riemer, N., West, M., Zaveri, R., & Easter, R. (2010). Estimating black carbon aging time-scales with a particle-resolved aerosol model. *Journal of Aerosol Science*, *41*(1), 143–158. https://doi.org/10.1016/j.jaerosci.2009.08.009

Riemer, N., West, M., Zaveri, R. A., & Easter, R. C. (2009). Simulating the evolution of soot mixing state with a particle-resolved aerosol model. *Journal of Geophysical Research: Atmospheres*, *114*(9), 1–22. https://doi.org/10.1029/2008JD011073

Rissler, J., Nordin, E. Z., Eriksson, A. C., Nilsson, P. T., Frosch, M., Sporre, M. K., et al. (2014). Effective density and mixing state of aerosol particles in a near-traffic urban environment. *Environmental Science and Technology*, *48*(11), 6300–6308. https://doi.org/10.1021/es5000353

Roelofs, G., Stier, P., Feichter, J., Vignati, E., & Wilson, J. (2006). Aerosol activation and cloud processing in the global aerosol-climate model ECHAM5-HAM. *Atmospheric Chemistry and Physics*, *6*(9), 2389–2399. https://doi.org/10.5194/acp-6-2389-2006

Romakkaniemi, S., Kokkola, H., Lehtinen, K., & Laaksonen, A. (2006). The influence of nitric acid on the cloud processing of aerosol particles. *Atmospheric Chemistry and Physics*, *6*(6), 1627–1634. https://doi.org/10.5194/acp-6-1627-2006

Roth, A., Schneider, J., Klimach, T., Mertes, S., Van Pinxteren, D., Herrmann, H., & Borrmann, S. (2016). Aerosol properties, source identification, and cloud processing in orographic clouds measured by single particle mass spectrometry on a central European mountain site during HCCT-2010. *Atmospheric Chemistry and Physics*, *16*(2), 505–524. https://doi.org/10.5194/acp-16-505-2016

Saliba, G., Chen, C. L., Lewis, S., Russell, L. M., Quinn, P. K., Bates, T. S., et al. (2020). Seasonal differences and variability of concentrations, chemical composition, and cloud condensation nuclei of marine aerosol over the North Atlantic. *Journal of Geophysical Research: Atmospheres*, *125*(19), 1–24. https://doi.org/10.1029/2020JD033145

Schell, B., Ackermann, I. J., Hass, H., Binkowski, F. S., & Ebel, A. (2001). Modeling the formation of secondary organic aerosol within a comprehensive air quality model system. *Journal of Geophysical Research: Atmospheres*, *106*(D22), 28275–28293. https://doi.org/10.1029/2001JD000384

Seinfeld, J. H., & Pandis, S. N. (2006). *From air pollution to climate change* (2nd ed.). John Wiley & Sons, Inc.

Shao, J., Chen, Q., Wang, Y., Lu, X., He, P., Sun, Y., et al. (2019). Heterogeneous sulfate aerosol formation mechanisms during wintertime chinese haze events: Air quality model assessment using observations of sulfate oxygen isotopes in Beijing. *Atmospheric Chemistry and Physics*, *19*(9), 6107–6123. https://doi.org/10.5194/acp-19-6107-2019

Shima, S., Kusano, K., Kawano, A., Sugiyama, T., & Kawahara, S. (2009). The super-droplet method for the numerical simulation of clouds and precipitation: A particle-based and probabilistic microphysics model coupled with a non-hydrostatic model. *Quarterly Journal of the Royal Meteorological Society*, *135*(642), 1307–1320. https://doi.org/10.1002/qj.441

Smith, J. D., Sio, V., Yu, L., Zhang, Q., & Anastasio, C. (2014). Secondary organic aerosol production from aqueous reactions of atmospheric phenols with an organic triplet excited state. *Environmental Science and Technology*, *48*(2), 1049–1057. https://doi.org/10.1021/es4045715

Sölch, I., & Kärcher, B. (2010). A large-eddy model for cirrus clouds with explicit aerosol and ice microphysics and lagrangian ice particle tracking. *Quarterly Journal of the Royal Meteorological Society*, *136*(653), 2074–2093. https://doi.org/10.1002/qj.689

Somers, J. (2004). Mobile source black carbon emissions, paper presented at Black Carbon Emissions and Climate Change: A Technical Workshop. U. S. Environmental Protection Agency, Washington, DC.

Stier, P., Feichter, J., Kinne, S., Kloster, S., Vignati, E., Wilson, J., & Petzold, A. (2005). The aerosol-climate model ECHAM5-HAM. *Atmospheric Chemistry and Physics*, *5*(4), 1125–1156. https://doi.org/10.5194/acp-5-1125-2005

Tilgner, A., Majdik, Z., Sehili, A. M., Simmel, M., Wolke, R., & Herrmann, H. (2005). SPACCIM: Simulations of the multiphase chemistry occurring in the FEBUKO hill cap cloud experiments. *Atmospheric Environment*, *39*(23-24), 4389–4401. https://doi.org/10.1016/j.atmosenv.2005.02.028

Unterstrasser, S., & Sölch, I. (2014). Optimisation of simulation particle number in a Lagrangian ice microphysical model. *Geoscientific Model Development*, *7*, 695–709. https://doi.org/10.5194/gmd-7-695-2014

Wagner, N. L., Brock, C. A., Angevine, W. M., Beyersdorf, A., Campuzano-Jost, P., Day, D., et al. (2015). In situ vertical profiles of aerosol extinction, mass, and composition over the southeast United States during SENEX and SEAC4RS: Observations of a modest aerosol enhancement aloft. *Atmospheric Chemistry and Physics*, *15*(12), 7085–7102. https://doi.org/10.5194/acp-15-7085-2015

Wang, Y., Ying, Q., Hu, J., & Zhang, H. (2014). Spatial and temporal variations of six criteria air pollutants in 31 provincial capital cities in China during 2013–2014. *Environment International*, *73*, 413–422. https://doi.org/10.1016/j.envint.2014.08.016

Winkler, P. (1973). The growth of atmospheric aerosol particles as a function of the relative humidity—II. An improved concept of mixed nuclei. *Journal of Aerosol Science*, *4*(5), 373–387. https://doi.org/10.1016/0021-8502(73)90027-X

Wolke, R., Sehili, A. M., Simmel, M., Knoth, O., Tilgner, A., & Herrmann, H. (2005). SPACCIM: A parcel model with detailed microphysics and complex multiphase chemistry. *Atmospheric Environment*, *39*(23-24), 4375–4388. https://doi.org/10.1016/j.atmosenv.2005.02.038

Wonaschuetz, A., Sorooshian, A., Ervens, B., Chuang, P. Y., Feingold, G., Murphy, S. M., & Jonsson, H. H. (2012). Aerosol and gas re-distribution by shallow cumulus clouds: An investigation using airborne measurements. *Journal of Geophysical Research: Atmospheres*, *117*(D17). https://doi.org/10.1029/2012jd018089

Ye, Q., Gu, P., Li, H. Z., Robinson, E. S., Lipsky, E., Kaltsonoudis, C., & Donahue, N. M. (2018). Spatial variability of sources and mixing state of atmospheric particles in a metropolitan area. *Environmental Science and Technology*, *52*, 6807–6815. https://doi.org/10.1021/acs.est.8b01011

Zaveri, R. A. (1999). A new lumped structure photochemical mechanism for large-scale applications. *Journal of Geophysical Research: Atmospheres*, *104*(D23), 30387–30415. https://doi.org/10.1029/1999JD900876

Zaveri, R. A., Barnard, J. C., Easter, R. C., Riemer, N., & West, M. (2010). Particle-resolved simulation of aerosol size, composition, mixing state, and the associated optical and cloud condensation nuclei activation properties in an evolving urban plume. *Journal of Geophysical Research: Atmospheres*, *115*(17), 1–19. https://doi.org/10.1029/2009JD013616

Zaveri, R. A., Easter, R. C., Fast, J. D., & Peters, L. K. (2008). Model for simulating aerosol interactions and chemistry (MOSAIC). *Journal of Geophysical Research: Atmospheres*, *113*(13), 1–29. https://doi.org/10.1029/2007JD008782

Zaveri, R. A., Easter, R. C., & Peters, L. K. (2005a). A computationally efficient Multicomponent Equilibrium Solver for Aerosols (MESA). *Journal of Geophysical Research: Atmospheres*, *110*(24), 1–22. https://doi.org/10.1029/2004JD005618

Zaveri, R. A., Easter, R. C., & Wexler, A. S. (2005b). A new method for multicomponent activity coefficients of electrolytes in aqueous atmospheric aerosols. *Journal of Geophysical Research: Atmospheres*, *110*(2), 1–23. https://doi.org/10.1029/2004JD004681

Zheng, Z., Curtis, J. H., Yao, Y., Gasparik, J. T., Anantharaj, V. G., Zhao, L., et al. (2021). Estimating submicron aerosol mixing state at the global scale with machine learning and earth system modeling. *Earth and Space Science*, *8*(2). https://doi.org/10.1029/2020ea001500